Kaon production in τ - decays

Erwin Agasi

Kaon production in τ - decays

ACADEMISCH PROEFSCHRIFT

TER VERKRIJGING VAN DE GRAAD VAN DOCTOR
AAN DE UNIVERSITEIT VAN AMSTERDAM
OP GEZAG VAN DE RECTOR MAGNIFICUS
PROF. DR. J.J.M. FRANSE
TEN OVERSTAAN VAN EEN DOOR HET COLLEGE
VOOR PROMOTIES INGESTELDE COMMISSIE
IN HET OPENBAAR TE VERDEDIGEN
IN DE AULA DER UNIVERSITEIT
OP 18 DECEMBER 2001 TE 10:45 UUR

door

Erwin Agasi

geboren te Heiloo

Promotor: *Prof. Dr. J.J. Engelen*
Co-promotor: *Dr. J.J.M. Timmermans*

Faculteit der Natuurwetenschappen, Wiskunde en Informatica

The work described in this thesis is part of the research program of 'het Nationaal Instituut voor Kernfysica en Hoge-Energie Fysica (NIKHEF)' in Amsterdam. The author was financially supported by 'de Stichting voor Fundamenteel Onderzoek der Materie (FOM)'.

Opgedragen aan Rosa, Isabel en Raúl

Contents

1 Introduction **5**

2 Theory **7**
2.1 Introduction 7
2.2 A brief look at the Standard Model 7
2.3 Effective Theory and cross sections 9
2.3.1 The decay $\tau \longrightarrow K\nu_\tau$ 10
2.3.2 Additional interactions in $\tau \longrightarrow K\nu_\tau$ 12

3 The DELPHI detector **15**
3.1 The LEP collider 15
3.2 Components of the DELPHI detector 16
3.3 Triggering and data handling 20

4 Electron identification with the HPC **23**
4.1 The detector 23
4.2 Signatures for electron identification with the HPC 25
4.3 Electron tagging with the HPC 28
4.4 Tuning the cuts 30
4.5 Summary and discussion 35
4.6 Conclusions 37

5 The Barrel Ring Imaging Cherenkov detectors in DELPHI **41**
5.1 Particle identification using Cherenkov radiation 41
5.2 The DELPHI barrel RICH 43
5.3 Performance study with di-muon events 46

6 Measurement of BR($\tau \rightarrow K\nu_\tau$) **55**
6.1 Event selection 55
6.2 Kaon identification with the RICH 60
6.3 Ring identification 62
6.4 Veto identification 64
6.5 The branching ratio BR($\tau \rightarrow K\nu_\tau$) 66
6.6 Conclusion 72

A Resonances in τ decays **75**

B The calculation of $\tau \to K\nu_\tau$ using a general Lorentz structure **79**

Bibliography **83**

Summary **87**

Samenvatting **89**

Acknowledgements **91**

Chapter 1

Introduction

The quest of mankind to explain all phenomena as interactions between basic constituents of matter, dates back many centuries: it ranges from the division into the basic building blocks of Earth, Water, Wood, Metal and Fire many centuries BC, to the division into the Proton, Neutron, Electron, Electron-neutrino and the Photon some fifty years ago and to the present day picture in which leptons and quarks play a fundamental role.

We learn about the way something is constructed by taking it apart, and reassembling it. It appears that the smaller the objects of study are, the more energy is needed to take them apart. Therefore, the deeper we probe into the world of the smallest particles, the more energy is needed. Experiments developed from tabletop size to the vast 27 km circumference accelerator near Geneva, Switzerland, with which we performed our measurements. High energy physics deals with the study of elementary particles and their interactions.

The analysis presented in this thesis deals with a specific class of decays of the heaviest lepton we know, the τ lepton. We measure the exclusive one prong kaon production in τ decays, i.e. $\tau \rightarrow K\nu_\tau$, where 'one-prong' stands for one charged particle in the final state. Because of its large mass of 1.8 GeV [1], the τ is the only lepton which can decay into hadrons. This feature provides us with a tool to study the coupling of leptons to hadrons, in particular, to confront the theoretical prediction for a specific decay rate with measurement.

In chapter 2, the current model of elementary particles and their interactions is briefly discussed. In Chapter 3, the DELPHI experiment is introduced and discussed. In the analysis presented in this thesis, we discriminate neutral particles from charged particles with the electromagnetic calorimeter of DELPHI. In chapter 4 this detector is described and methods for identifying electrons are discussed. In our experiment, we used the Ring Imaging Cherenkov (RICH) detector of DELPHI to identify kaons on a track-by-track basis. The design, the working principle and the performance of the RICH are discussed in chapter 5. In chapter 6, the τ event selection is discussed. The

[1] Throughout this thesis we used the convention $\hbar = c \equiv 1$.

particle identification of our final data sample using the RICH is described and results are given for two identification methods. Then, the final results on the branching ratio $\tau \rightarrow K\nu_\tau$ are presented, and a comparison is made with other results on the branching ratio $\tau \rightarrow K\nu_\tau$.

Chapter 2

Theory

2.1 Introduction

In present day experimental high energy physics, the main goal is to investigate the still unverified aspects of the very succesful theory of electromagnetic, weak and strong interactions. The model we have for describing these interactions is known as the Standard Model. So far, experimental results have shown excellent agreement with predictions of this model. However, there are indications that this model is not the final word. For instance, it does not predict the masses of elementary particles and the number of generations of fundamental fermions. Moreover, gravitation is not incorporated in the model.

A number of extensions of the Standard Model are under consideration to provide explanations for these questions. So far, no experimental indications have been found on the direction to follow. One approach to find such indications is through the study of rare processes at energies now available. The topic of this thesis, single prong kaon production in τ decays, focusses on one of these processes.

The Standard Model is formulated as a gauge field theory. In the following sections the Standard Model prediction for single prong kaon production in τ decays is given, and possible effects of physics beyond the Standard Model are discussed.

2.2 A brief look at the Standard Model

The Standard Model is described by the $U_Y(1) \otimes SU_L(2) \otimes SU_C(3)$ groups. The $U_Y(1) \otimes SU_L(2)$ group describes the electro-weak interactions. Masses are introduced by spontaneous breaking of the $SU_L(2)$ symmetry. $U_Y(1)$ mixes with $SU_L(2)$, one unbroken generator remains and is identified as the photon, the other three generators are broken and become massive. They are the Z^0, W^- and W^+ bosons, the carriers of the weak force. The gauge fields needed to retain $SU_C(3)$ invariance are called gluons. There are eight gluons and they are the mediators of the strong force.

Generation			Quantum numbers		
I	II	III	Q	T	T_3
$\begin{pmatrix} \nu_e \\ e \end{pmatrix}_L$	$\begin{pmatrix} \nu_\mu \\ \mu \end{pmatrix}_L$	$\begin{pmatrix} \nu_\tau \\ \tau \end{pmatrix}_L$	0 -1	$\frac{1}{2}$ $\frac{1}{2}$	$\frac{1}{2}$ $-\frac{1}{2}$
e_R	μ_R	τ_R	-1	0	0
ν_{eR}	$\nu_{\mu R}$	$\nu_{\tau R}$	0	0	0
$\begin{pmatrix} u \\ d' \end{pmatrix}_L$	$\begin{pmatrix} c \\ s' \end{pmatrix}_L$	$\begin{pmatrix} t \\ b' \end{pmatrix}_L$	$\frac{2}{3}$ $-\frac{1}{3}$	$\frac{1}{2}$ $\frac{1}{2}$	$\frac{1}{2}$ $-\frac{1}{2}$
u_R	c_R	t_R	$\frac{2}{3}$	0	0
d_R	s_R	b_R	$-\frac{1}{3}$	0	0

Table 2.1: The three generations of the Standard Model. The charge Q is expressed in units of elementary charge. T is the weak isospin. Included are the righthanded neutrino's but we note that they do not participate in electroweak interactions.

The gauge fields enter in the covariant derivative which reads in general:

$$D_\mu = \partial_\mu + ieA_\mu Y + \frac{i}{2}g\mathbf{B}_\mu \cdot \sigma + ig_s\mathbf{G}_\mu \cdot \Lambda \tag{2.1}$$

where Y is the hypercharge ($Q = T_3 + \frac{1}{2}Y$), σ the generators for $SU(2)$ and Λ those for $SU(3)$. The fields A_μ, B_μ and G_μ are the gauge bosons needed to retain $U_Y(1)$, $SU_L(2)$ and $SU_C(3)$ invariance. They stand for the photon field, boson field and gluon field respectively. The subscript s in g_s denotes strong interaction. See for an explicit formulation of the total Lagrangian for instance [1].

In table 2.1, the three generations of fundamental fermions are listed per multiplet with their quantumnumbers. We note that the quarks in table 2.1 are the $SU_L(2)$ eigenstates. The $SU_L(2)$ doublet for quarks is $\bar{L} = \left(\bar{u}\ \bar{d}'\right)_L$, where the prime indicates a linear combination of mass eigenstates. The transformation between the two different bases, i.e. between $SU_L(2)$ and the real mass eigenstates (d, s and b) , is given by the Cabibbo-Kobayashi-Maskawa matrix:

$$\begin{pmatrix} d' \\ s' \\ b' \end{pmatrix} = \begin{pmatrix} V_{ud} & V_{us} & V_{ub} \\ V_{cd} & V_{cs} & V_{cb} \\ V_{td} & V_{ts} & V_{tb} \end{pmatrix} \begin{pmatrix} d \\ s \\ b \end{pmatrix} \tag{2.2}$$

The Cabibbo-Kobayashi-Maskawa matrix is unitary and complex. The four matrix elements in the upper left corner can be approximated by:

$$\begin{pmatrix} d' \\ s' \end{pmatrix} = \begin{pmatrix} \cos\theta_C & \sin\theta_C \\ -\sin\theta_C & \cos\theta_C \end{pmatrix} \begin{pmatrix} d \\ s \end{pmatrix} \tag{2.3}$$

The 2×2 matrix thus obtained has one degree of freedom, the angle θ_C. This angle is known as the Cabibbo angle and plays a crucial role in the analysis presented in this thesis [2].

2.3 Effective Theory and cross sections

In this section we will calculate hadronic decay rates of the τ lepton, the decay of for instance τ to K is depicted in figure 1(a). Hadrons are particles which consist of quarks.

The rate of a decay can be expressed as follows:

$$d\Gamma = \frac{1}{E_d} |\mathcal{M}|^2 (2\pi)^4 \delta^4 (\sum_f p_f - p_d) \prod_f \frac{dp_f}{(2\pi)^3 2E_f} \tag{2.4}$$

where the subscript f denotes all final state particles, d the decaying particle and the matrix element $\mathcal{M}$ contains the details of the process involved. The general form for a decaying τ is:

$$\mathcal{M} \simeq G_F \bar{\nu_\tau} \gamma^\alpha \left(1 + \gamma^5\right) \tau J_\alpha \tag{2.5}$$

where $\bar{\nu_\tau} \gamma^\alpha (1 + \gamma^5) \tau = \bar{\nu_\tau} (\gamma^\alpha - \gamma^5 \gamma^\alpha) \tau$ represents the charged current connected with the τ and J^α denotes the current it couples to. This coupling is known as the V-A coupling, referring to vector (γ^α) and axial vector ($\gamma^5 \gamma^\alpha$) couplings. We note that:

$$\bar{\nu_\tau} \gamma^\alpha \left(1 + \gamma^5\right) \tau = \bar{\nu_\tau} \frac{1}{2} \left(1 - \gamma^5\right) \gamma^\alpha \left(1 + \gamma^5\right) \tau = 2 \bar{\nu_\tau}_L \gamma^\alpha \tau_L \tag{2.6}$$

This term comes directly from $\bar{L} \not{D} L$ where L is the lepton doublet. The hadronic current J^α can be found from (2.6) by the substitutions $\bar{\nu_\tau} \rightarrow u$ and $\tau \rightarrow \bar{d'}$. Remember that [2]

$$\bar{d'} = V_{ud} \bar{d} + V_{us} \bar{s} = \cos\theta_C \bar{d} + \sin\theta_C \bar{s} \tag{2.7}$$

This leads to the introduction of the Cabibbo angle θ_C in the decay rate[3]. The constant G_F in (2.5) is called the Fermi constant. This constant can be expressed as:

$$G_F = \sqrt{2} \frac{g^2}{8 m_W^2} \tag{2.8}$$

The actual coupling of a W to a $u\bar{s}$ charged current can be calculated. However, it is not a free $u\bar{s}$ pair which is formed, but a quark anti-quark state which is called a meson. It is not clear how to calculate this bound state from first principles. We therefore need an effective description for the coupling of the W to the meson.

[2] We neglect the third generation quarks.

[3] $\sin\theta_C \approx 0.23$

Spectral function	Spin-Parity	Strangeness	Decay channel
a_0	0^-	0	π^-
a_1	1^+	0	$a_1^-(1260)$
v_1	1^-	0	$\rho^-(770), \rho(1700)$
a_0^s	0^-	-1	K^-
a_1^s	1^+	-1	$K_1^-(1270), K_1^-(1400)$
v_1^s	1^-	-1	$K^{*-}(892)$

Table 2.2: Quantum numbers of τ decay channels

Four years before the actual discovery of the τ lepton, Tsai [3] systematically calculated all hadronic modes of the τ decay. The coefficients a and v are spectral functions depending on the squared momentum of the final state particles, q^2.

For the total hadronic decay width for the τ we obtain:

$$\begin{aligned}\Gamma(\tau \rightarrow hadrons + \nu_\tau) &= \frac{G_F^2}{32\pi^2 m_\tau^3} \int_0^{(m_\tau - m_\nu)^2} dq^2 (m_\tau^2 - q^2)^2 \times \\ &\Big\{ cos^2\theta_C \Big[(m_\tau^2 + 2q^2)(v_1(q^2) + a_1(q^2)) + m_\tau^2 (v_0(q^2) + a_0(q^2)) \Big] + \\ &sin^2\theta_C \Big[(m_\tau^2 + 2q^2)(v_1^s(q^2) + a_1^s(q^2)) + m_\tau^2 (v_0^s(q^2) + a_0^s(q^2)) \Big] \Big\}\end{aligned} \tag{2.9}$$

where the a and v denote axial-vector and vector parts, the superscript s denotes strangeness and the subscripts indicate the spin of the hadron. In table 2.2 the quantum numbers are given together with the possible decay modes.

2.3.1 The decay $\tau \longrightarrow K\nu_\tau$

In this thesis we are concerned with one prong hadronic decays of the τ lepton. A one prong decay is a decay with one charged track in the final state. The most interesting channel is $\tau \longrightarrow K\nu_\tau$. This decay is Cabibbo suppressed, which means that the coupling of the W to the K involves terms of $\sin^2\theta_C$ where the Cabibbo allowed decay into π has $\cos^2\theta_C$. Relative to the Cabibbo allowed decay, the suppressed channel has a very low rate ($\tau \longrightarrow \pi\nu_\tau : \tau \longrightarrow K\nu_\tau \simeq 20 : 1$). Therefore any additional interaction which is not present in the current model, will affect the Cabibbo suppressed decay relatively more than the Cabibbo allowed decay. Both the coupling of the W to the $u\bar{s}$ charged current and the formation of the two quark bound state are hidden in the coupling f_K. By definition, this factor f_K is also present in the process $K \longrightarrow \mu\nu_\mu$, see figure 2.1. To be more specific, both matrix elements $\mathcal{M}$ are identical and Γ differs only in phase space. By taking the ratio of the two rates, the factor f_K cancels and enables a precise calculation of exclusive kaon production in τ decays. Although the

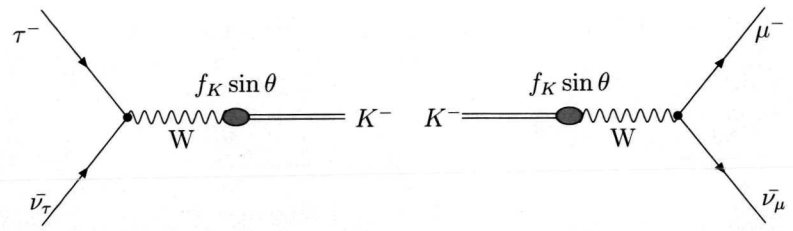

(a) τ decays to a kaon (b) Kaon decays to a muon

Figure 2.1: Feynman diagrams of weak decays

precision with which we can calculate this process turns out to be much higher than we can presently achieve experimentally, we can set a limit on additional interactions. The $\tau \longrightarrow K\nu_\tau$ width is found by substituting

$$a_0^s(q^2) = 2\pi f_K \delta(q^2 - m_K^2) \tag{2.10}$$

into equation (2.9) and yields:

$$\Gamma(\tau \to K\nu_\tau) = \frac{1}{16\pi} G_F^2 f_K^2 \sin^2\theta_C m_\tau^3 \left(1 - \frac{m_K^2}{m_\tau^2}\right)^2 \tag{2.11}$$

As mentioned before, the process $K \longrightarrow \mu\nu_\mu$ is similar to $\tau \longrightarrow K\nu_\tau$ apart from phase space factors. The rate is given by:

$$\Gamma(K \to \mu\nu_\mu) = \frac{1}{8\pi} G_F^2 f_K^2 \sin^2\theta_C m_\mu^2 m_K \left(1 - \frac{m_\mu^2}{m_K^2}\right)^2 \tag{2.12}$$

The relation between the width Γ and the branching ratio BR is given by:

$$\Gamma_i = \frac{1}{\tau} BR_i \ , \ \tau = \left(\sum_i \Gamma_i\right)^{-1} \tag{2.13}$$

for some decay i. By taking the ratio of equations (2.11) and (2.12), we find:

$$BR(\tau \to K\nu_\tau) = \frac{1}{\tau_K} \times \tau_\tau \times BR(K \to \mu\nu_\mu) \times f(m_\mu, m_K, m_\tau) \tag{2.14}$$

Here, $f(m_\mu, m_K, m_\tau)$ follows from taking the ratio. It is a function of the particles masses only and is given in appendix B. Decker and Finkemeier calculated radiative corrections for the ratio [4]:

$$R_{\tau/K} = \frac{\Gamma(\tau \to K\nu_\tau)}{\Gamma(K \to \mu\nu_\mu)} \tag{2.15}$$

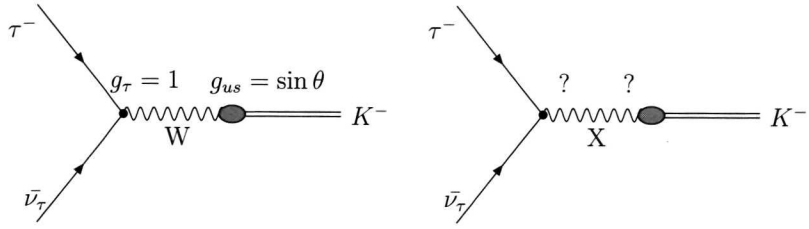

(a) Standard Model interaction (b) A different scenario

Figure 2.2: Standard Model couplings and extensions

and found $\delta R_{\tau/K} = (0.90 \pm 0.22) \cdot 10^{-2}$. Here, the parameter $\delta R_{\tau/K}$ is defined by:

$$R_{\tau/K} = R^0_{\tau/K}\left(1 + \delta R_{\tau/K}\right) \tag{2.16}$$

where the superscript 0 denotes the prediction without radiative corrections. Other uncertainties come from the lifetime measurements and the branching ratio measurement of $K \to \mu\nu_\mu$.

Inserting the lifetimes, the branching ratio $BR(K \to \mu\nu_\mu)$, and the masses of the particles in f, we find:

$$BR(\tau \to K\nu_\tau) = 0.72 \pm 0.01\% \tag{2.17}$$

2.3.2 Additional interactions in $\tau \longrightarrow K\nu_\tau$

The determination of the branching ratio $\tau \to K\nu_\tau$ enables us to identify or to set a limit on additional interactions. This is done by again calculating the ratio (2.15). This time, the calculation is led by the most general principles. Instead of the V-A Lorentz structure described in the previous section, we added an interaction with a general Lorentz structure in $\mathcal{M}$. In appendix B the details of the calculation are given. The result of the calculation can be compared with the ratio (2.15) found by substituting the measured values in the numerator and denominator. This leads to a limit on additional interactions as we will see.

The physical interpretation of the general Lorentz structure is that we allow any boson to propagate between the τ and the ν_τ on one side and the K on the other side as shown in figure 2.2. Of course, the same scenario applies for the case $K \to \mu\nu_\mu$. In our derivation we considered spin 0 and spin 1 bosons with different vector axial-vector couplings.

For the specific decays we are interested in, the difference between a spin 0 or a spin 1 boson is that the latter introduces factors m_τ and m_μ for the numerator and denominator of equation (2.15) respectively (see appendix B).

We investigated three scenario's, they are an additional interaction of the normal V-A Lorentz structure, a V+A Lorentz structure and a pure V or A Lorentz structure. The following relations apply:

V-A:

$$R_{\tau/K} = \left(1 + 2\frac{g'_{us}}{\sin\theta_C}(g'_{\tau} - g'_{\mu})\right) f(m_{\mu}, m_K, m_{\tau}) \tag{2.18}$$

V+A:

$$R_{\tau/K} = \left(1 + \left(\frac{g'_{\tau} g'_{us}}{\sin\theta_C}\right)^2 - \left(g'_{\mu} g'_{us}\right)^2\right) f(m_{\mu}, m_K, m_{\tau}) \tag{2.19}$$

Pure V or A:

$$R_{\tau/K} = \left(1 + \frac{g'_{\tau} g'_{us}}{\sin\theta_C} - \sin\theta_C g'_{\mu} g'_{us}\right) f(m_{\mu}, m_K, m_{\tau}) \tag{2.20}$$

The factors g'_{us}, g'_{τ} and g'_{μ} denote couplings to the new boson, the effect of which is enhanced by the $\sin\theta_C$ in the denominator. By inserting the value for f and the measured value for R, we can set a limit on the combination of the new couplings as given above.

Chapter 3

The DELPHI detector

3.1 The LEP collider

DELPHI is one of the four experiments at the Large Electron Positron collider (LEP) at CERN, Geneva. LEP is an accelerator and storage ring for counter rotating bunches of electrons and positrons with a circumference of 26.7 km located at a depth of about 100 m. In figure 3.1 a schematic view of the location of the accelerator and the four

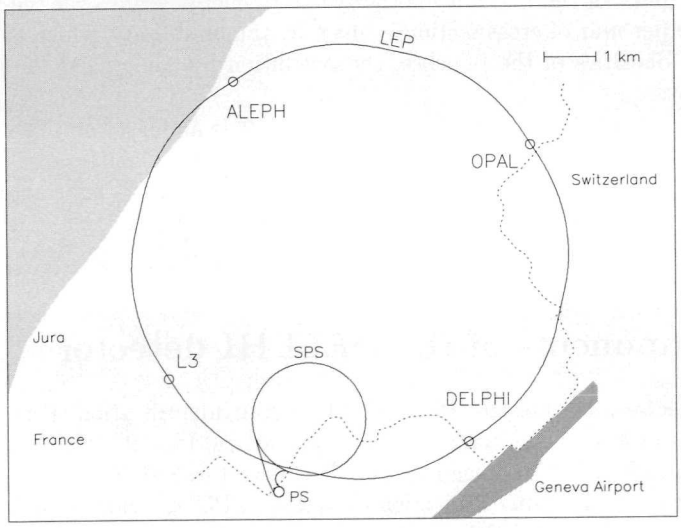

Figure 3.1: LEP and the PS/SPS injector chain configuration

Year	L in pb^{-1}	Mode	hadronic Z^0's
1990	6.5	scan	125 k
1991	10.0	scan	275 k
1992	24.0	peak	751 k
1993	35.3	scan	755 k
1994	47.5	peak	1484 k
1995	33.5	scan	750 k
Total	156.8		4140 k

Table 3.1: Integrated luminosities (L) taken by DELPHI since the start of LEP

detectors is given.

Depending on the mode of operation, the electron and positron beams in the accelerator each consist of four or eight discrete bunches. They collide in four points. In four bunch mode, the bunch crossing frequency is about 45 kHz. In other words, there is a 22 μs period between successive bunch crossings. At each interaction point a detector is installed: L3, Aleph, Opal and DELPHI.

In the first phase of LEP operation, electrons and positrons are collided at centre-of-mass energies close to the Z^0 resonance (about 45 GeV per beam). If an electron and positron annihilate, they make a Z^0 at rest. Some years have been dedicated to running at the peak of the resonance, other years to energy scans over the resonance. The event rate per unit of cross section is given by the luminosity, which is a function of the particle densities of the bunches, the revolution frequency and the size of the crossing bunches.

The peak cross section for the process $e^+e^- \longrightarrow Z^0$ is about 44 nb. The number of Z^0's produced is found by multiplying the cross section with the integrated luminosity. The Z^0's decay for about 70 % (about 31 nb) to hadrons, 10 % to charged leptons, and the remaining 20 % decay to neutrino pairs, invisible for the detectors. In table 3.1 integrated luminosities taken by DELPHI and collected Z^0's are listed per year.

3.2 Components of the DELPHI detector

DELPHI -DEtector with Lepton, Photon and Hadron Identification- (see figure 3.2) is a general purpose detector with emphasis on particle identification. To this end DELPHI is equiped with Ring Imaging Cherenkov detectors (RICH). Ionisation energy loss measurements in the Time Projection Chamber (TPC) provide an additional way of identifying particles in DELPHI.

DELPHI is a cylindrical detector. It has a barrel part and two end caps. All barrel detectors form concentric cylindrical shells around the beam axis. The DELPHI coor-

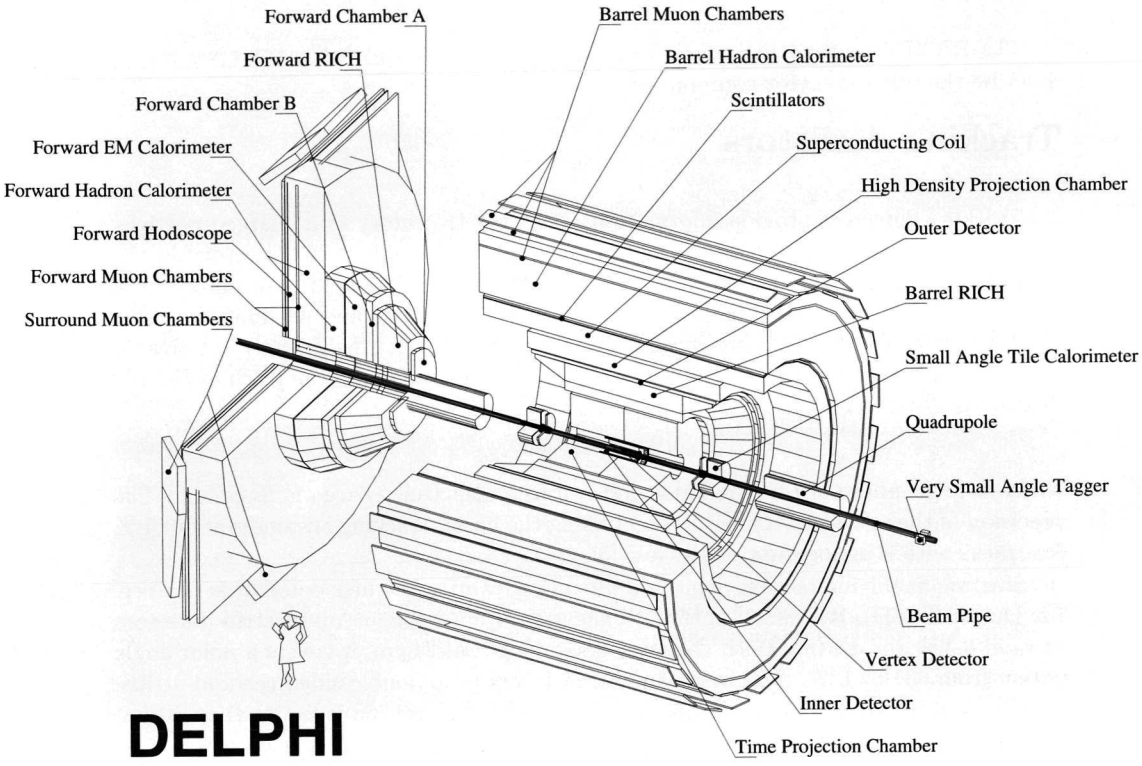

Figure 3.2: Schematic view of the DELPHI detector

dinate system is such that the z-axis coincides with the beam-axis where the positive z runs in the direction of the e^- beam. The x-axis is perpendicular to the z-axis and is directed to the centre of the ring, the y-axis is perpendicular to the x- and z-axes to complete a right handed coordinate system.

The RICH detector is described in detail in chapter 5. In this chapter we briefly describe the other detector components.

Tracking detectors

Tracking detectors provide information about the trajectory of a charged particle. The operation is based on ionisation. The curvature of a particle's trajectory in the DELPHI magnetic field is used to obtain its momentum. The field is produced by a superconducting solenoid. The solenoid has a length of 7.4 m and an inner diameter of 5.2 m. The field strength produced is 1.2 T. In the magnetic field, charged particles will follow a helical trajectory. If r is the radius of curvature and ζ the pitch angle, the relation is given by:

$$p\cos\zeta = 0.3Br \tag{3.1}$$

where p is given in GeV, B in Tesla and r in meters. Unit charge is assumed. The precision of the momentum measurement using the barrel tracking system is about 1 % for tracks with a momentum of 10 GeV [5].

Starting at the interaction point and moving outwards, the first detector is the Vertex Detector (VD). It consists of three concentric layers of silicon micro strip detectors at radii 6.3, 9 and 11 cm. With the outer layer length of 24 cm, it covers a polar angle region from 43° to 137°. The inner and outer layers have double-sided readout strips, providing both $R\phi$ and z measurements. The single hit precision is better than 10 μm in $R\phi$ and of the same order for z.

From radii 12 cm to 28 cm the Inner Detector (ID) is located. It consists of two parts: a jet chamber and a set of trigger layers outside the jet chamber. The jet chamber is subdivided in 24 sectors in $R\phi$, each subtending 15°. Every sector has 24 sense wires, measuring drift times in $R\phi$ direction. The single wire resolution varies from 75 μm to 125 μm. The resolution of a local track element in the Inner Detector is 50 μm in $R\phi$ and 1.5 mrad in ϕ.

The five trigger layers are cylindrical multi-wire proportional chambers (MWPC's) with 192 anode wires parallel to the beam axis and 192 circular cathode strips perpendicular to the beam. Single plane resolution along the beam-axis varies from 0.5 to 1 mm for well isolated tracks depending on the angle of the track. A track-finding chip performs pattern recognition on hit combinations in the five layers. It plays an important role in the formation of the DELPHI trigger decision. There are 8 chips per 15° sector.

From 1995 onwards, a new Inner Detector has been operational. First results indicate a single wire resolution of 85 μm. The resolution of a local track element in the new Inner Detector is 40 μm in $R\phi$ and 0.89 mrad in ϕ [5].

From radii 29 cm to 122 cm, the Time Projection Chamber (TPC) is situated. The chamber is divided in two halves by a high voltage plate at $z = 0$ (the interaction point is located at $z = 0$). In both directions in z, the detector extends 130 cm. In $R\phi$, the detector is divided in six sectors. When a particle traverses a sector, it ionises the drift gas. Electrons drift to the end plates. There, they create an avalanche on the sense wires (192 per sector, they offer a measurement of dE/dx), and induce a signal on the cathode read out pads located behind the sense wires. There are 16 circular rows of pads, so up to 16 space points per track can be reconstructed. Each sector contains 1680 pads which allow a measurement in $R\phi$ with a single point resolution of about 250 μm. The resolution in z is close to 1 mm.

The outer detector (OD) ranges from 198 cm to 206 cm in R. It consists of 24 sectors in azimuth. Each sector measures 470 cm in z and contains 145 drift tubes in five layers. The layers are staggered in order to ensure a full coverage in azimuth. All layers give $R\phi$ information. The three middle layers also give z information by relative timing of signals at both ends. This fast z measurement is used in the trigger. The single point resolution in $R\phi$ is 110 μm per track, the precision in z around 4 cm.

The barrel muon chambers (MUB) are located on the outside of DELPHI. They are arranged in three layers with full coverage in azimuth. Each separate layer contains multiple planes of drift chambers. Free electrons drift maximally 10 cm to an anode wire. Time differences between the signals at each end of the chamber provide a z measurement. The muon chambers measure about 3.7 m in z. The resolution obtained is 1.5 mm in $R\phi$ and about 1.0 cm in z.

In the two forward regions, tracking is done by the Forward Chambers A (FCA), Forward Chambers B (FCB) and the Forward Muon Chambers (MUF). Typical resolutions of the A and B chambers are about 300 μm in x and y. For the forward muon chambers the resolution is of the order of 1 mm.

Calorimeters

DELPHI is equipped with two kinds of calorimeters, electromagnetic calorimeters and hadron calorimeters.

In the barrel region the electromagnetic calorimeter (HPC) is a gas sampling calorimeter. The detector itself is described in detail in the next chapter. The resolution

obtained is parametrised as follows:

$$\frac{\sigma_E}{E} = 0.043 \oplus \frac{0.32}{\sqrt{E}[\text{GeV}]}$$

The forward electromagnetic calorimeter (FEMC) covers polar angles between 10° and 36.5° and between 143.5° and 170°. The detector is made out of lead glass blocks shaped in truncated pyramids, pointing towards the interaction region. Its resolution is about 6.5 % for Bhabha's ($e^+e^- \rightarrow e^+e^-$) at 46 GeV.

Two other electromagnetic calorimeters are found in the forward direction, the Small Angle tagger (SAT) and the Very Small Angle tagger (VSAT). The SAT is the luminosity monitor, consisting of alternating sheets of lead and scintillating fiber. In 1994 it was replaced by the Small angle TIle Calorimeter (STIC) with similar spatial and energy resolution, but with larger angular coverage.

DELPHI is equipped with a HAdron Calorimeter (HAC) using iron as absorber. The calorimeter is incorporated in the return yoke of the magnet. The calorimeter is placed in the barrel as well as in the end caps. Polar angle coverage extends from $11.2° - 48.5°$, $42.6° - 137.4°$ and $131.5° - 168.8°$. The detector is again a gas sampling calorimeter. It has 20 layers of limited streamer mode detectors of thickness 2 cm. The absorber layers are 5 cm thick iron plates. The resolution obtained with this detector is

$$\frac{\sigma_E}{E} = 0.21 \oplus \frac{1.12}{\sqrt{E}[\text{GeV}]}$$

3.3 Triggering and data handling

DELPHI has three levels of triggering. The first and second level trigger (T1 and T2) decisions are made 3 μs and 40 μs after the beam crossover (BCO). Decisions are based upon information coming from subdetectors. This information is sent to subtriggers. All subtrigger data are collected in one module: the trigger supervisor. The final trigger decision is made by a logical combination of all subtriggers. The following subtriggers are used in the process:

- Track subtrigger
- Muon subtrigger
- electromagnetic energy subtrigger

- Hadronic energy subtrigger
- Bhabha subtrigger

Detectors which provide this information are the inner detector(ID), the outer detector(OD), the time projection chamber (TPC), the time of flight detectors (TOF and HOF), muon chambers and the electromagnetic and hadron calorimeters. The first and second level triggers are implemented in hardware.

The third level trigger T3 is purely a software trigger. Its task is to bring the final trigger rate down to a few Hz. Typical processing time for the T3 is about 30 ms. After T3, events are written to tape.

The vast amount of data collected by the detector is processed using the DELPHI data reconstruction package DELANA [6]. This package contains routines for all detectors as submodules. Local pattern recognition is performed and later integrated in global event information.

All relevant detector parameters (geometry, temperatures, voltages, etc.) are recorded online and put in a database. This database is called by DELANA during event reconstruction. The DELANA output is written to Data Summary Tapes (DST's). They serve as the starting point for physics analysis.

Chapter 4

Electron identification with the HPC

4.1 The detector

The High-density Projection Chamber (HPC) is the barrel electromagnetic calorimeter of DELPHI. It is a sampling calorimeter with a depth of about 18 radiation lengths. By means of a gas-sampling technique, it provides a measurement of the energy deposited by a traversing particle, in three dimensions and with high granularity. Sheets of lead cause the traversing particles to interact which results in a shower of particles. The shower particles ionise gas molecules. The ionisation charges drift towards proportional readout chambers. The collected charge provides a measure of the energy of the incident particle.

The HPC is a cylinder with inner and outer radii of 208 and 255 cm. The total length in z measures 500 cm. The detector is subdivided in 24 sectors in ϕ and 6 sectors in z, combining to a total of 144 independent modules.

An HPC module consists of 41 layers of lead, spaced by 8 mm gaps. The volume between the lead layers is filled with drift gas: an 80 % argon / 20 % methane mixture. The lead layers consist of a fiberglass-epoxy support on which thin lead wires are glued. A resistor chain is used to provide a voltage gradient between neighbouring lead wires, yielding a drift field of about 100 Volts/cm in z. The ionisation charges drift to readout chambers.The chambers are single-plane Multi Wire Proportional Chambers (MWPC). The segmented cathode layer consists of 8 mm by 8 mm U-shaped brass elements. The sense wire is a 20 μm gold plated wire. The cathode elements are grouped into 128 pads. The pattern is shown in figure 4.1.

Information about the z-coordinate is obtained by drift time measurements. The amplified charge is sampled at 15 MHz. The sampling frequency combined with an average drift velocity of 5.5 cm/μs gives a granularity of about 3.7 mm.

The HPC has ten layers in depth. The fourth layer consists of a plane of scintillators and is dedicated to triggering. The HPC yields a granularity of 1 degree in ϕ and

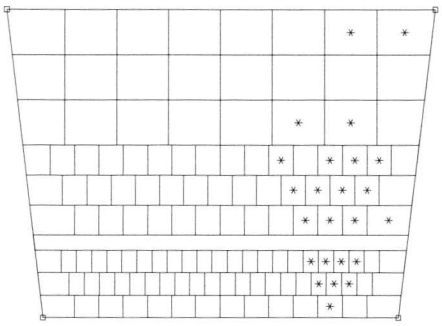

Figure 4.1: Pad layout of the MWPC, the stars depict a typical shower of a traversing electron.

nine samples in depth.

The construction of the HPC does not allow full solid angle coverage. In between adjacent modules there are about 1 cm wide cracks. There are two kinds of cracks, ϕ-cracks and θ- or z-cracks. The ϕ-cracks point to the interaction region. Particles do shower in ϕ-cracks but most information is lost in the dead material. Only tails of the shower are seen in the calorimeter and shower information can only be deduced indirectly. The θ-cracks are less problematic. Particles coming from the interaction point traverse θ-cracks only for a small segment of the track. They then enter the calorimeter again. In this case, part of the information is lost but the measurement is corrected for this effect in the analysis.

Since the HPC is a gas sampling calorimeter, the energy resolution is not particularly good. However, the spatial granularity is very good and provides a good three dimensional reconstruction of the deposited energy, which is deposited in a narrow cone. This enables one to distinguish between different decay products of the τ. The HPC is particularly well suited for separating electrons from other decay products. This will be discussed in the next sections.

4.2 Signatures for electron identification with the HPC

The analysis described in this thesis is for a large part based on particle identification with the RICH detector. Since kaon production in τ decays is strongly suppressed, great care has to be taken to avoid misidentification. Electrons are a source of misidentification. They interact easily with the material of the detector, leading to deflections of the original trajectory of the electron, the emission of photons, or even the production of showers in front of the RICH. Another source of misidentification are K^*'s. If the photons due to a π^0 from a K^* decay are not detected, or the energy deposited by the photons in the HPC are not associated with the charged track, a K^* will be identified as a kaon. With a single set of cuts based on the HPC measurements, both electrons and K^*'s are effectively rejected. This will be explained when we discuss our event selection for the study of exclusive one prong kaon production in τ decays in chapter 6.

On the other hand, if we want to measure the inclusive one prong kaon production in τ decays ($\tau \rightarrow K\nu_\tau + n\pi^0$, $n \geq 0$), we have to distinguish between electrons and π^0's. Since a small fraction of misidentified electrons can significantly influence the branching ratio measurement, the electrons have to be efficiently vetoed. Therefore, the electron tag must be designed for high rejection efficiency and only to a lesser extent for low impurity.

In this chapter, we describe the development of an electron tag which fulfills this requirement. To this end, we used two sets of data. One set consists of KORALZ[7] generated $e^+e^- \rightarrow \tau^+\tau^-$ events which passed all τ selection cuts except the HPC cuts. The selection cuts are described in chapter 6. The other set consists of real data taken in 1994. The real data set is subjected to the same set of cuts as the one applied to the simulated events. The electron identification cuts we will introduce and apply in this section, are taken sequentially. It is understood that when we discuss a certain cut, the cuts discussed previously are already in effect.

The ratio E/p

The HPC measures the electromagnetic energy E deposited by a traversing particle. Together with the momentum measurement p in DELPHI, the ratio E/p can be determined. With this variable, distinction can be made between electrons and minimum ionising particles.

Electrons produce electromagnetic showers, and their energy is completely absorbed in the HPC: the ratio E/p for electrons will peak around the value 1. Muons, pions and kaons however, are minimum ionising in the HPC and the ratio E/p will therefore be much lower. This is shown in figure 4.2. A cut on the E/p ratio does, however, not reject efficiently the τ decays with neutral pions in the final state. In case $\tau^- \longrightarrow \rho^-\nu_\tau$,

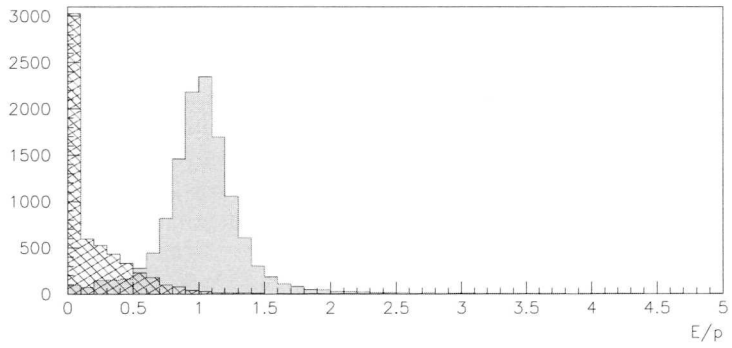

Figure 4.2: The ratio of energy over momentum for electrons(shaded) and pions(hatched) from selected τ decays. The data is taken from KORALZ simulated events with full detector simulation.

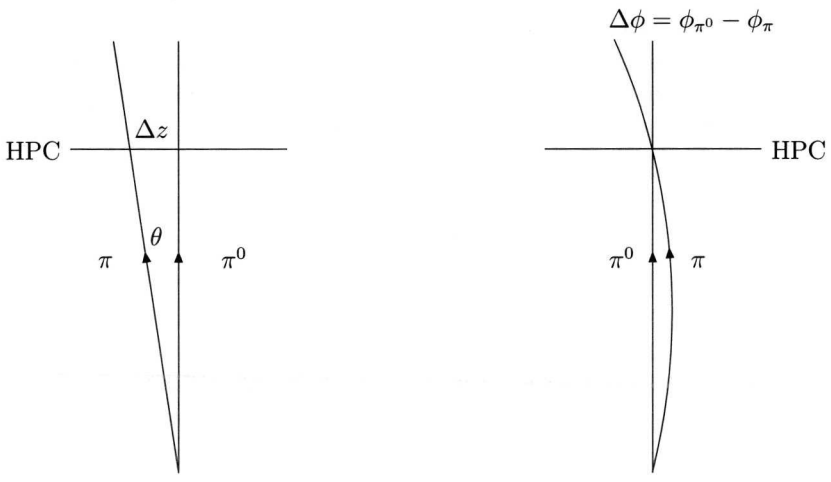

(a) A ρ decay in R-z view

(b) A ρ decay in Rϕ view

Figure 4.3: ρ decay products entering the HPC

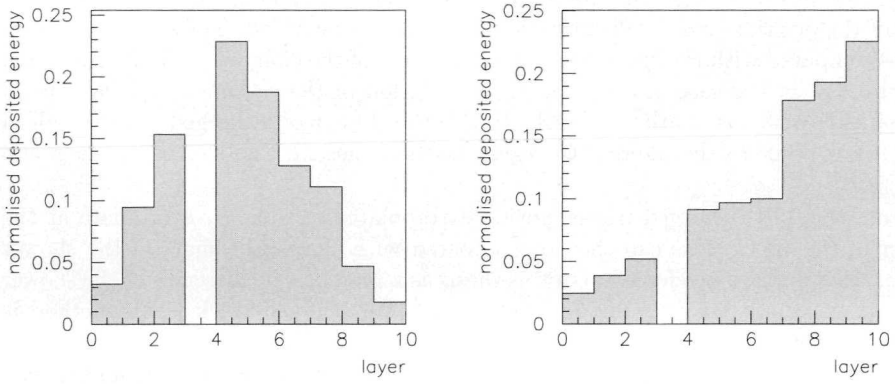

(a) Longitudinal shower profile for electrons

(b) Longitudinal shower profile for pions

Figure 4.4: Shower profiles for electrons and pions. The fourth bin or layer in this plot corresponds to a plane of scintillators used for triggering purposes. It therefore has no entries.

the ρ decays to a π^- and a π^0. The π^0 in turn decays to two photons that produce showers in the HPC. The charged track bends in the magnetic field whereas the neutral track is not deflected. For a small opening angle $\Delta\phi$ (figure 4.3), the energy deposition of the neutral is attributed to the charged track. If the π^- and π^0 have similar energy, this will lead to an E/p ratio around 1. For that reason, τ decays with neutrals in the final state, are not as effectively cut as the exclusive one prong τ deacys.

Longitudinal shower profile

The nine samples in depth can be used to construct a longitudinal shower profile, i.e. the deposited energy as a function of the distance traversed in the calorimeter. Again, this can be used to distinguish showering particles from minimum ionising particles. An electron or photon will lose its energy gradually in an electromagnetic shower. This leads to a smooth longitudinal shower profile, peaking in the first layers of the HPC. In contrast, large energy deposits of pions in the HPC are due to strong interactions. Often, the bulk of the energy is then found deeper in the calorimeter as compared to electrons. Therefore, the shower profile for electrons and minimum ionising particles differs considerably, which is shown in figure 4.4.

Position and direction of the shower

Because of the high granularity and the sampling technique used, a good measurement of the position and the direction of the showers is provided. These measurements can be compared with the corresponding parameters of the charged track fit. As shown in figure 4.3, in the case of a ρ^- decay, the position of the π^0 shower will in general not coincide with that of the π^- track. In Rϕ, the shower of a charged particle will in general not point to the interaction region because the track is bent in the magnetic field.

From the TPC, charged tracks can be extrapolated to give a z-coordinate at the border of the HPC. This can then be compared with the z-coordinate of the shower centre. This method is referred to in this thesis as z-match. The direction of the shower in ϕ can be compared with the direction in ϕ of the charged track. This method is addressed as ϕ-match in this thesis.

The z- and ϕ-match both enable us to distinguish an electron from minimum ionising particles accompanied by neutrals. Note, however, that for small opening angles θ (see figure 4.3), this method becomes less sensitive. After applying the E/p cut, the z-match is expected to show the best separation power. The angular resolution is about 0.6 mrad in θ for electrons. This corresponds to 1.3 mm in z at the border of the HPC for a track with a polar angle of 90°. In ϕ the position resolution is 6.5 mm at the border of the HPC, corresponding to 3.1 mrad. For high energy photons the directional resolution is 1.0 mrad and 1.7 mrad in θ and ϕ respectively. The ϕ-match serves in our analysis primarily to separate ρ's from electrons. In order to resolve the difference between the direction of charged π and the π^0 coming from the ρ, one needs a curvature of the charged track corresponding to a p_T of no more than 1 GeV. The momentum of the particles we select in this analysis is too high to expect the ϕ-match criterium to be effective.

4.3 Electron tagging with the HPC

The general DELPHI software incorporates a very broad package called Elephant [8]. This package provides refined calibration of the HPC, corrections on the measured energy in case particles traverse cracks in the detector, and other corrections. Also, the quantities discussed in the previous section are calculated. Together with third stage pattern recognition they form the basic elements of an electron tag.

The electron tag in Elephant is tuned on hadronic Z^0 decays. These decays are characterised by high multiplicity and low momentum tracks. In the present analysis we study τ decays into one charged particle which has much higher momentum. Furthermore, the analysis of the inclusive one prong kaon production requires a high efficiency for electron tagging. In this chapter, a method for electron tagging is presented which is optimised for the needs in the τ analysis. The method is, as we will see, partly based on the quantities described in the previous section.

The criteria for tagging electrons in τ decays are straightforward. The relatively clean environment in τ decays allows a study of efficiency versus purity of the electron tag, by simply tuning a few cut values. This is not the case for the tag provided by Elephant where quite sophisticated methods are used to reach a high purity electron sample. Elephant provides three electron tags: the loose tag, the standard tag and the tight tag.

In addition to the tagging quantities shower profile, E/p, the z-match and the ϕ-match, the Elephant package provides a comparison with the electron hypothesis by calculating probabilities. The advantage of using a probability rather than the quantity itself is illustrated with the example of the E/p ratio. The E/p distribution depends on the momentum of the track. A low momentum electron bends considerably in the magnetic field of DELPHI. Photons which are radiated off can be detected well outside the region of energy deposition attributed to the track. This effect leads to a tail at low E/p values. On the other hand, a high momentum electron which is scattered, can be attributed a lower momentum, leading to a tail at high E/p values. The probability calculated by Elephant takes this momentum dependence into account. For all quantities which were discussed earlier, probabilities are calculated [5].

We use the individual probabilities given in the Elephant package and tune the cut values to find the optimal tag for our analysis. Our tag then forms a four (i.e. the shower profile, E/p, the z-match and the ϕ-match) dimensional cube in probability space. Mathematically the most elegant way to design an electron tag is to combine all probabilities into an overall probability. Necessary and sufficient constraints are that the variables should be independent and should have a flat probability spectrum for electrons only. When this last criterium is not met, the variable under consideration does not follow a normal distribution.

In experiments however, one does not encounter ideal distributions. By an incorrect estimate of the error, the variables will follow a non-normal distribution. Also, because all four quantities are derived from the same detected hits, correlations are expected. Correlations can introduce systematic effects and weaken the overall performance of the single tagging variable. We therefore discard the idea of combining probabilities, and use the separate probabilities instead.

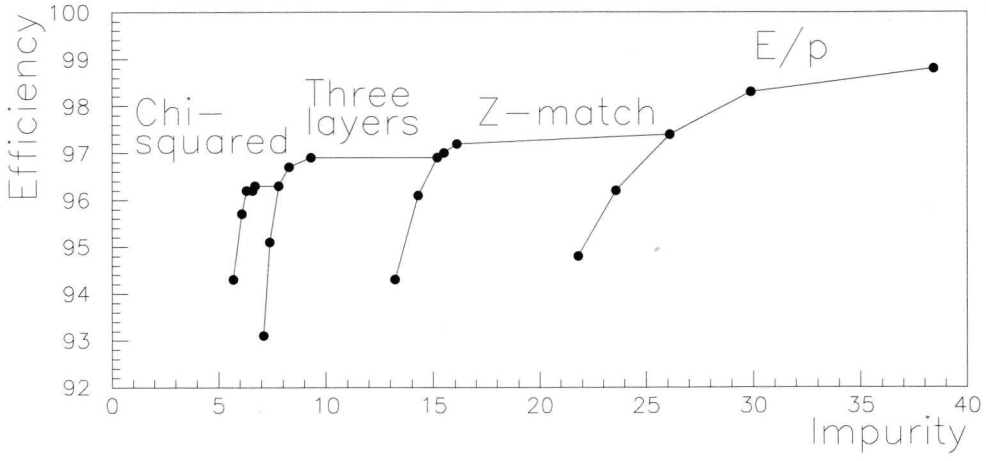

Figure 4.5: Trading purity against efficiency: the path to an optimal electron tag.

4.4 Tuning the cuts

The optimal electron tag is found by setting the cut values on the tagging variables such that an optimal ratio between efficiency and impurity is found. The efficiency is defined as:

$$\text{Efficiency} = \frac{\text{number of electrons selected by the cuts}}{\text{total number of electrons}} \times 100\% \qquad (4.1)$$

The impurity is defined as:

$$\text{Impurity} = \frac{\text{number of non-electrons selected by the cuts}}{\text{total number of particles selected by the cuts}} \times 100\% \qquad (4.2)$$

The route to our electron tag is shown in figure 4.5: bring a cut on a new tagging variable into effect when the separation power of the previous tagging variable lessens. The objective is to stay as close as possible to the upper left corner of the plot. All particles have passed the τ selection cuts (chapter 6). In particular they have a momentum between 4 GeV and 25 GeV. The plots which are shown contain only particles which traversed no cracks. In a similar way, the cuts are tuned for particles traversing cracks.

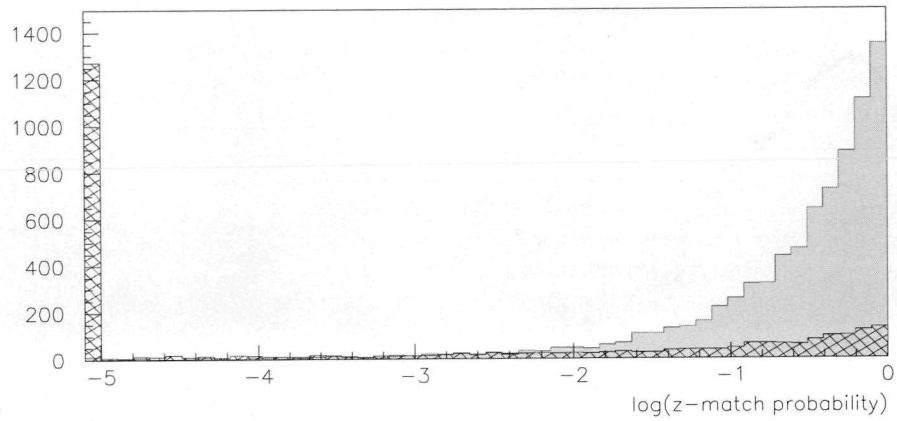

Figure 4.6: z-match probability for electrons (shaded) and non-electrons (hatched).

We studied the probabilities based on E/p, shower profile, z - match and ϕ - match. The most important variable of this set, and therefore the first variable to cut on, is the probability based on the ratio E/p. Indeed, the E/p variable is the only variable in which the total deposited energy enters. All other variables are more sophisticated derivations from the HPC measurement. If the energy measurement is incorrect, the other variables will surely not perform better. The cut value for the E/p based probability was set to 0.05. This corresponds to an efficiency of 97.4 % and an impurity of 26.1 % of our electron sample. The numbers are taken from simulated events.

The next variable to cut on is the probability based on the z-match. This variable is expected to show the best separation power after the E/p cut is applied. The distribution is shown in figure 4.6. From the figure one finds that quite some background can be cut away almost without affecting the efficiency. The cut on this probability was set to the value of 0.0001. Together with the cut on the E/p based probability, this yielded an efficiency of 96.9 % and an impurity of 15.2 %.

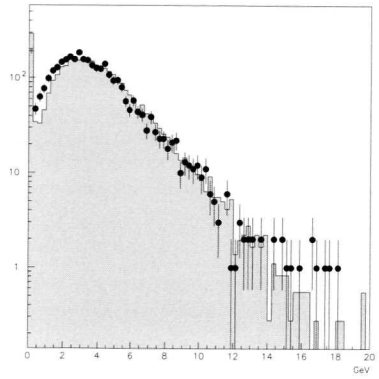

Figure 4.7: The energy deposition in the first three layers of the HPC for real events (dots) and simulated events (shaded).

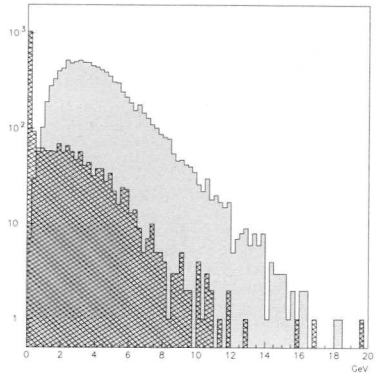

Figure 4.8: The energy deposition in the first three layers of the HPC for electrons (shaded) and non-electrons (hatched).

A feature of electromagnetically interacting particles is that they will lose a substantial amount of their energy in the first few layers of the HPC. This in contrast to strongly interacting particles. A selection criterium for electrons would be the amount of energy deposited in the layers before the trigger layer, i.e., in the first three layers of the HPC. In figure 4.7 the distribution of the deposited energy in the first three layers for real data and KORALZ simulation are plotted. In figure 4.8 the same distributions are separately given for electrons and non-electrons, taken from simulated events. Clearly, this provides an excellent handle to bring the background in the electron sample down. The cut value was set to 0.5 GeV, together with the cuts on the E/p and z-match probabilities this yielded already an efficiency of 96.4 % and an impurity of 7.8 %.

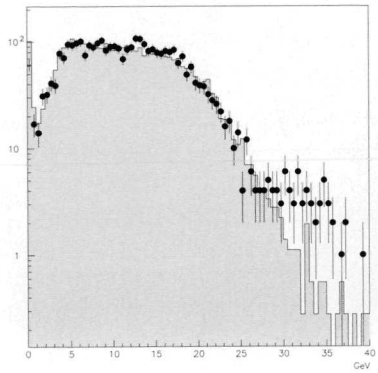

Figure 4.9: The energy deposition in the first six layers of the HPC for real events (dots) and simulated events (shaded).

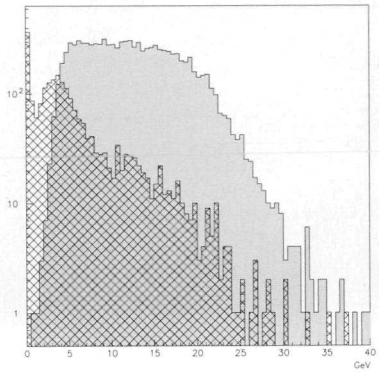

Figure 4.10: The energy deposition in the first six layers of the HPC for electrons (shaded) and non-electrons (hatched).

In case the particle traversed cracks in the HPC, we used the energy deposition of the first six layers where the layer with the least amount of energy was omitted. The comparison between real events and simulated events and the distributions for electrons and non-electrons are shown in figures 4.9 and 4.10. To produce this figure, we used the data from tracks traversing no cracks to obtain enough statistics.

We studied the probability based on the shower profile and found that the impurity could not be brought down without losing 10 % on our efficiency. Puzzled by the poor performance of the shower profile probability, we started checking the energy distributions over all layers for electrons which were given a low probability. The cause was a relatively large energy deposit in one or more of the last three layers.

We therefore developed an alternative shower profile where the aforementioned anomaly was ruled out. The problem we mentioned was countered by only summing over the first six layers [1]. The variable we designed is a normalized χ^2 test quantity;

$$\chi^2 = \frac{1}{6}\sum_{i=1}^{6}\left(\frac{\hat{E}_i - \hat{E}_{exp,i}}{\sigma_i}\right)^2 \tag{4.3}$$

where $\hat{E}_i$ and $\hat{E}_{exp,i}$ are the measured and expected energy in the first six layers, divided by the total energy deposited in the first six layers. σ_i is the width of the normalised

[1] The fourth layer is dedicated to triggering and therefore does not enter the definition of the first six layers

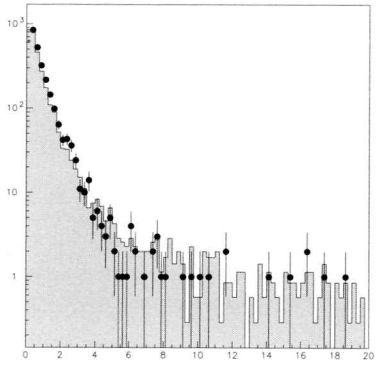

Figure 4.11: The χ^2 test quantity (horizontally) for real events (dots) and simulated events (shaded).

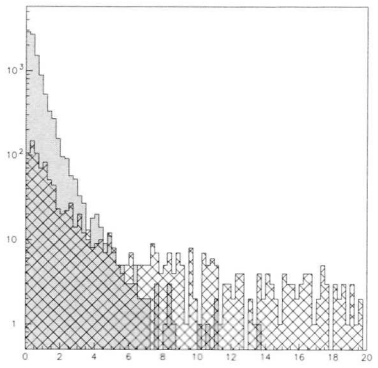

Figure 4.12: The χ^2 test quantity (horizontally) for electrons (shaded) and non-electrons (hatched).

energy distribution of the i-th layer. The expected energy per layer and the σ per layer are taken from simulated events.

Both the measured energy and the expected energy per layer were scaled with the total energy measured. No effort was made to incorporate momentum dependence. The distributions for real events and simulated events and the separation between electrons and non-electrons are shown in figures 4.11 and 4.12.

We put the cut on our χ^2 test quantity at the value 6. The χ^2 cut combined with the cuts on the E/p based probability, the z-match probability and the cut on the minimum amount of energy in the first three layers, it yields an overall efficiency of 96.3 % and an impurity of 6.4 %. At the end of this chapter, cut values and efficiencies are given for all regions, non-, θ- and ϕ-cracks.

We end this section by noting that a cut on the presence of neutrals in the decay would effectively cut away the ρ's and a_1's from the electron sample. Such a cut however, would cut away about 10 % of the electrons because of radiative τ decays and is therefore not applied.

	No cuts	P(E/p)	P(z-match)	Three layer cut	Chi-squared
$e^{\pm}$	100 %	97.4 %	96.9 %	96.4 %	96.3 %
$\mu^{\pm}$	100 %	0.1 %	0.1 %	0.0 %	0.0 %
$\pi^{\pm}$	100 %	7.8 %	5.9 %	2.0 %	1.6 %
$\rho^{\pm}$	100 %	15.8 %	8.2 %	3.8 %	3.0 %
$a_1^{\pm}$	100 %	21.6 %	9.0 %	5.2 %	4.4 %
$K^{\pm}$	100 %	10.3 %	7.0 %	3.7 %	1.6 %
$K^{*\pm}$	100 %	28.2 %	4.4 %	2.9 %	2.9 %

Table 4.1: Contributions of different decay channels in the simulated event sample after the various (successive) cuts.

4.5 Summary and discussion

In this section, we discuss the influence of the previously described cuts on the different one prong decay channels. All quoted numbers apply to selected one prong τ decays where the charged track has a momentum between 4 and 25 GeV. Tracks pointing to cracks were removed.

As can be seen from table 4.1, the cut on E/p drastically cuts away almost all muons and reduces the π and K channels by a factor of ten. The cuts are less efficient in removing the ρ's, a_1's and the K^*'s. This was to be expected. Indeed, these resonances decay into one charged track (multi prongs are ignored) and one or more neutrals. In principle a ρ should behave under this cut as a π. In some cases however, the neutral energy becomes attributed to the charged track. This is even more the case for $K^* \rightarrow K\pi^0$. Studies on simulated events of the opening angle between the K and π^0 compared with the opening angle between the π and π^0 coming from a ρ, showed a larger contribution at small opening angles for K^*'s.

As described in section 4.2, resonances can be distinguished using the granularity of the HPC. With the cut on the z-match based probability the resonances are effectively reduced to below ten percent.

The cut on the energy deposited in the first three layers reduces the π content with almost a factor three. The decays where neutrals are involved are reduced by a factor of two.

	No cuts	P(E/p)	P(z-match)	Three layer cut	Chi-squared
$e^{\pm}$	24.2 %	74.0 %	84.8 %	92.2 %	93.6 %
$\mu^{\pm}$	22.3 %	0.1 %	0.1 %	0.0 %	0.0 %
$\pi^{\pm}$	11.9 %	2.9 %	2.5 %	0.9 %	0.8 %
$\rho^{\pm}$	27.0 %	13.4 %	8.0 %	4.1 %	3.2 %
$a_1^{\pm}$	9.6 %	6.5 %	3.1 %	2.0 %	1.7 %
$K^{\pm}$	0.7 %	0.2 %	0.2 %	0.1 %	0.1 %
$K^{*\pm}$	0.6 %	0.5 %	0.1 %	0.1 %	0.1 %

Table 4.2: Relative contributions of different decay channels in the simulated sample after the various (successive) cuts. Note that only the most important one prong decay channels are taken into account. For this reason the columns do not add up to precisely 100 %.

The sample is further purified with the cut on the χ^2. As can be seen from table 4.1, the percentage of π's, ρ's and a_1's is further brought down by a factor 0.8. Since we do not want to cut on the presence of neutrals in the decay, the ρ's and a_1's which are still left in the sample behave as π's under the χ^2 cut. The effect of the cut at this stage is not very big. In table 4.2 the relative contributions of the different one prong decay channels are listed as a function of the various cuts. From this table we see that the contamination from other decay channels after all the cuts amounts to 6 % in total.

	No cracks	θ cracks	ϕ cracks
P(E/p) >	0.05	0.01	0.001
P(z-match) >	0.0001	0.0001	0.0001
$E_{3layers}$ >	0.5 GeV	-	-
$E_{6layers}$ >	-	1.0 GeV	1.0 GeV
χ^2 <	6.0	6.0	6.0
$E_{neutral}$ <	-	2.0 GeV	1.0 GeV
Efficiency	96.3 %	90.9 %	69.4 %
Impurity	6.4 %	6.8 %	7.0 %

Table 4.3: Summary of all cuts

Summarising we give the various cuts, efficiencies and impurities for all regions in table 4.3. In the less efficient regions (cracks), the cut parameters are slightly altered. This is especially the case for the cut on the E/p variable which is loosened in the crack regions. In order to further improve the electron rejection in the cracks, we added a cut on the neutral energy deposited in a 20° cone around the track. The neutral energy was weighted with the inverse distance to the track. This cut is not applied in the no-crack region because it cuts away too much signal (the non-electrons).

4.6 Conclusions

We designed an electron tag with the aid of HPC information only. The overall efficiency amounts to 91.7 %, and in 6.5 % of the cases other particles are mistakenly identified as electrons. The overall efficiency is calculated by separating the sample according to the traversed regions, i.e. no cracks, θ- and ϕ- cracks. Then, the particle was tagged using the cuts which were described earlier. The performance of the electron tag can be improved by introducing the energy-loss measurement in the TPC. For several cut values on the energy-loss based probability, the efficiency and impurity were determined. The result is shown in figure 4.13. The standard, loose and tight

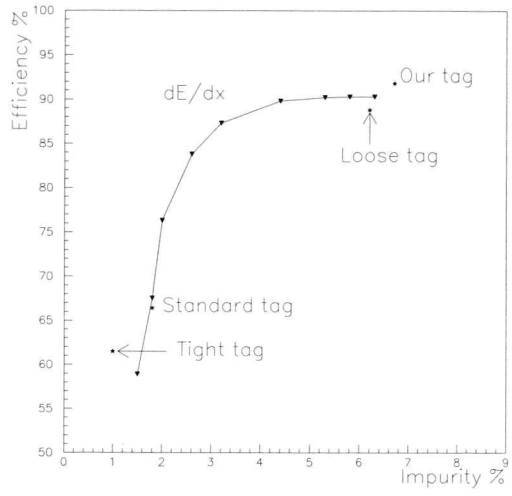

Figure 4.13: Performance of the several electron tags. The curve is obtained by including in our electron tag a cut on the probability based on the energy-loss measurement, and connecting the points for several cut values on this probability.

	Our tag	Loose tag	Standard tag	Tight tag
Efficiency	91.7 %	88.8 %	66.4 %	61.5 %
Impurity	6.5 %	6.2 %	1.8 %	1.0 %

Table 4.4: Overall efficiencies of the various electron tags

tags from the Elephant package are shown for comparison.

Efficiencies and impurities for all tags are summarised in table 4.4. The values in the column 'our tag' were obtained by use of HPC information only.

From the numbers the difference in philosophy between our approach and that of the Elephant team is clearly depicted. We want to identify as many electrons as possible whereas the Elephant tags enable one to obtain a very pure electron sample. The purity as provided by the Elephant tags can be obtained by bringing in the energy-loss measurements from the TPC or tightening the already existing cuts.

Another important difference is that the behaviour of the tag performance as a function of cut variables involved is known, as given in figure 4.13. This enables one to change the performance easily when necessary.

Of the particles mistakenly tagged as electrons, the bulk consists of ρ's, a_1's and pions. Considering the original number of these particles, less than 5 % of the population will be lost when the electron tag is used as a veto, as can be seen from table 4.1.

Chapter 5

The Barrel Ring Imaging Cherenkov detectors in DELPHI

5.1 Particle identification using Cherenkov radiation

When a particle traverses a transparent medium with index of refraction n, and if the velocity of the particle satisfies

$$\beta > \frac{1}{n}, \text{ where } \beta = \frac{v}{c}, \tag{5.1}$$

it will radiate photons. This is called the Cherenkov effect [9]. Together with a measurement of the momentum of the particle, equation (5.1) leads to the following constraint on the mass of a particle emitting Cherenkov radiation:

$$m < p\sqrt{n^2 - 1} \tag{5.2}$$

where the relations $p = \gamma m\beta$ and $\gamma = (1 - \beta^2)^{-1/2}$ are used.

Two particles with equal momentum but with different mass, can be distinguished by designing a detector in which one particle radiates Cherenkov photons while the other one does not. Detectors like this are called threshold Cherenkov counters.

The photons are emitted under a well defined angle θ_C, the Cherenkov angle, with respect to the direction of flight of the particle:

$$\cos\theta_C = \frac{1}{\beta n} \tag{5.3}$$

By measuring θ_C and combining this with the measurement of the momentum, equation (5.3) leads to a determination of the mass of the particle:

$$m = p\sqrt{n^2 \cos^2\theta_C - 1} \tag{5.4}$$

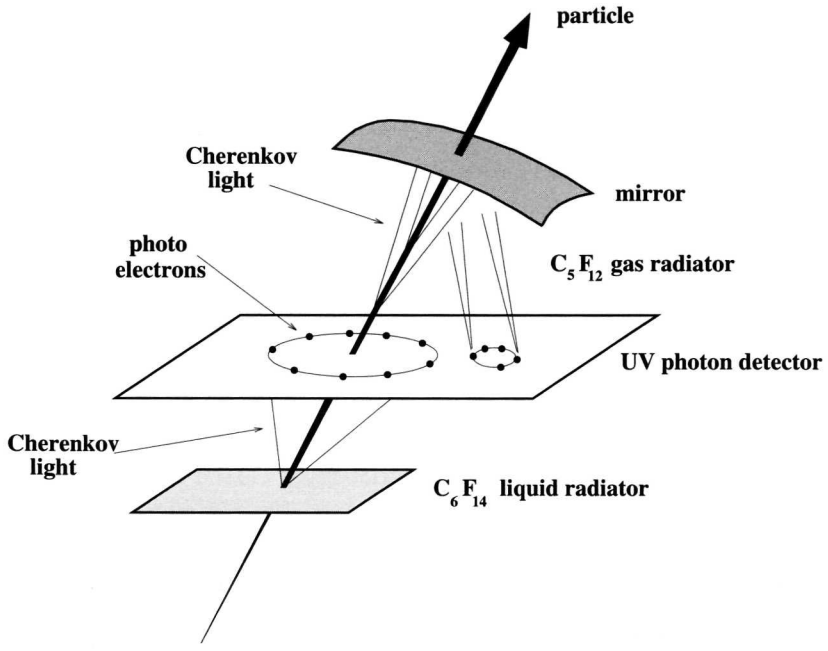

Figure 5.1: Schematic view of the barrel RICH working principle

The working principle of the DELPHI Cherenkov detector is illustrated in figure 5.1. A particle traverses first a liquid C_6F_{14} radiator. If equation (5.1) is satisfied, it will radiate photons in a cone around the track. The image of the cone is measured in a UV photon detector, where the photons are converted into photo-electrons. After having traversed the photon detector, the particle enters the gas radiator, which is a volume filled with the gas C_5F_{12}. The gas has a lower index of refraction than the liquid. The photons emitted in the gas radiator are projected back onto the UV photon detector by focussing mirrors. The projected image of the cone is a ring whose radius is proportional to the Cherenkov angle θ_C. The use of two radiators increases the momentum range for particle identification considerably. This is illustrated in table 5.1.

In this chapter, we will use the terms 'veto identification' and 'ring identification' which we will explain here. In the analysis presented in this thesis, we are concerned with identifying kaons. In τ decays at LEP, kaons are produced with a minimal mo-

	C_6F_{14}	C_5F_{12}
e	0.0006 GeV	0.0086 GeV
μ	0.13 GeV	1.8 GeV
π	0.17 GeV	2.4 GeV
K	0.62 GeV	8.4 GeV
p	1.2 GeV	16.1 GeV

Table 5.1: Cherenkov thresholds for particles in C_6F_{14} and C_5F_{12}

mentum of about 3.5 GeV. Since the Cherenkov threshold for kaons is 8.4 GeV in the gas radiator, we distinguish two momentum regions. One momentum region is from 3.5 GeV to 8.4 GeV, where the kaon does not radiate Cherenkov photons in the gas radiator. This region is called the veto region and the method of particle identification is similar to that of a Cherenkov threshold counter. The other region is from 8.4 GeV upwards. Here, the angle θ_C is measured for all particles, this region is referred to as the ring identification region. Pions start radiating at 2.4 GeV. In order to suppress background in the veto region for kaons, we will select only particles with momentum higher than 4 GeV in this thesis. We define 4 GeV as the threshold for veto identification and 9 GeV as the threshold for the ring identification region. However, we note that there is a small overlap in momentum between veto and ring identification due to the fact that the identification method also depends on the angle θ of the track (determining the length of the trajectory in the gas radiator) and the momentum. The analysis is explained in detail in the next chapter.

5.2 The DELPHI barrel RICH

The Barrel RICH (BRICH) is a 3.5 m long cylinder with inner and outer radii of 124 cm and 197 cm respectively. It is divided into two halves by a 6.4 cm thick wall, located at z = 0. The mid wall is made of a honeycomb structure clad by epoxy resin and glass fiber mats.

Each half is divided into 24 sectors in azimuth. Each sector contains a liquid radiator, a photon detector which is a drift tube with a Multi Wire Proportional Chamber (MWPC), and a set of six mirrors. The gas radiator fills the remaining volume.

In figure 5.2 the longitudinal cross section of the BRICH is shown. A particle coming from the interaction point enters the RICH through the inner cylinder wall. This is a 15 mm mylar/polyurethane insulator wound on a aluminum honeycomb cylinder. Immediately behind the inner cylinder, liquid radiator trays are located. A tray contains 1 cm of C_6F_{14} and is closed by a 4 mm thick UV-grade quartz window. Around

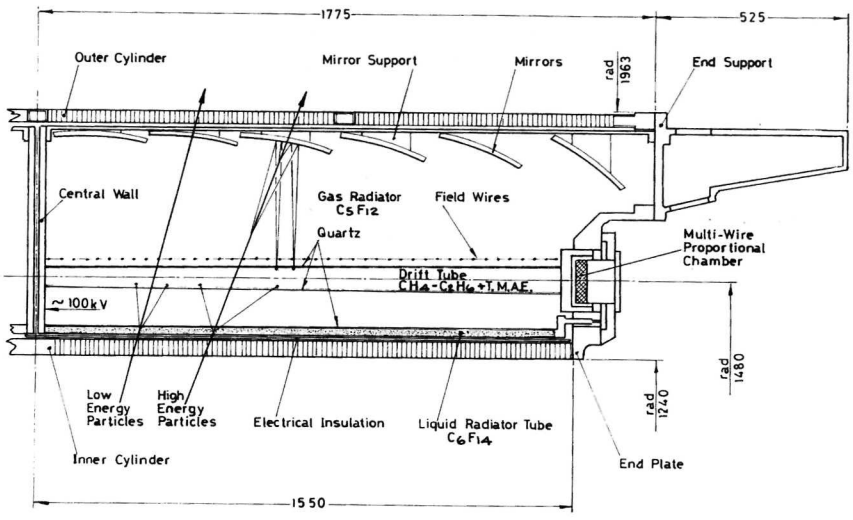

Figure 5.2: Lay-out of the barrel RICH detector. Only one quarter of the longitudinal cross-section is shown.

the tray there are $130\mu m$ wide metallic strips with a pitch of 6 mm in z. They help to provide a well defined electrical field within the detector. The distance between the liquid radiators and the drift tube is about 11 cm.

A drift tube measures about 155 cm in z, it is 34.5 cm wide and the depth varies from 4.2 to 6.2 cm, increasing away from the interaction point. The structure is made this way to avoid efficiency losses in electron transport close to the walls of the drift tube, due to diffusion. The windows of the drift tube are made of UV-grade quartz. As a photo-sensitive agent, TMAE [1] was chosen. Combined with the quartz windows, it allows for a photon conversion in the energy range of about 5.6 - 7.4 eV. The lower limit corresponds to the ionization potential of the TMAE. The upper limit is due to photon absorption in the quartz. The TMAE has been added to a driftgas mixture of 75/25 % CH_4/C_2H_6. On the surface of the drift tube, metallic strips are mounted. They have a pitch of 3 mm in z. A resistor chain supplies the voltage gradient needed for the drift field. The photo-electrons drift maximally 155 cm to the MWPC's mounted on the end of the drift tubes. To provide a good single photon detection, drift attenuation lengths of more than 5 m are realised. The MWPC's have an anode wire pitch of 2.62 mm, the wires enable an $r\varphi$ measurement. The cathode strip pitch is about 4 mm; it measures the conversion depth. The z-coordinate is calculated through the measured drift time

[1] Tetrakis-diMethylAminoEthylene

and the drift velocity.

Apart from the photo-electrons from Cherenkov photon conversions, the MWPC's register free electrons which come from the ionisation of the driftgas caused by the traversing particle. The ionization hits are used in the analysis to determine if the drift tube was operational.

Between the top of the drift tubes and the outer cylinder of the BRICH, there is 39 cm of C_5F_{12} gas; the gasradiator. Focussing mirrors are mounted on the outer cylinder. The mirrors focus the Cherenkov photons from the gas radiator such, that the projection onto the drift tubes is a ring.

Among the many parameters to be monitored in the BRICH, temperature is one of the most important. The BRICH operates at a temperature of 40° C. The boiling temperature of C_5F_{12} is about 29° C and the TMAE concentration corresponds to its vapor pressure at 28° C. If the temperature drops too much, these gases will condense. A deposit of TMAE would damage the drift tubes severely.

Fluctuations in the temperature will also cause fluctuations in the drift velocity and this will consequently lead to mismeasurements of the Cherenkov angle. Furthermore, since thermal expansion directly leads to misalignment for all detector components within the BRICH, stability of temperature is necessary.

Therefore, the BRICH is equipped with a sophisticated heating system. On both the outer and inner cylinder heating strips are mounted. These strips are driven by 32 power supplies. The temperature is monitored by 245 temperature probes. The detector is thermally insulated from the rest of DELPHI to avoid heat dissipation. Furthermore, a number of safety measures as alarm and interlock systems, automatic purges and several back-up computer systems are installed.

The BRICH is equipped with an online calibration system to monitor the drift velocity. Per drift tube, a 9×5 matrix of quartz fibers is installed. It consists of rows of nine fibers at five different locations in z. The fibers are driven by a UV-lamp located outside the DELPHI detector. The lamp is triggered by Bhabha events. The frequency is about 0.3 Hz and the accuracy on the drift velocity thus obtained is 0.02 %. For a more complete documentation on the BRICH and the alignment, we refer to [10].

5.3 Performance study with di-muon events

To ensure a correct projection of the Cherenkov photons onto the drift tube, the detector has to be properly aligned. One of the aspects of the alignment process concerns the mirror system. The mirrors are aligned by minimizing the spread in the Cherenkov angle for a sample of high momentum (straight) tracks. We used a sample of di-muon events, i.e. $Z^0 \rightarrow \mu^+\mu^-$, for the alignment. The di-muon sample is selected by requiring exactly two charged collinear tracks, where both tracks have a momentum compatible with the beam energy, and a low deposition of electromagnetic energy. The muon momentum of 45 GeV provides an almost straight track through the detector as well as a maximal number of Cherenkov photons emitted at the saturated Cherenkov angle, which is 61.5 mrad for the gas radiator.

The location and direction of the track's trajectory in the radiator, together with the position of the Cherenkov photons on the drift tube, are used to calculate the angle under which Cherenkov photons are emitted. To ensure a correct determination of the Cherenkov angle, cuts are made on the quality of the track. Therefore, the track has to have elements in both the TPC and the Outer Detector. Interpolation of these track elements will give the trajectory traversed in the barrel RICH. Since the barrel RICH is divided in two by a mid-wall, the polar region from 86° to 94° is cut out because of reduced efficiency.

Bad sectors or runs are identified by checking the number of ionization hits along the track in the drift tube. For instance, high voltage trips may cause a sector to become temporarily non-operational and no ionization hits are detected. We require that a track should have at least two ionization hits in the drift tube. With this constraint, about 10 % of the good tracks are discarded. The loss is mainly attributed to particles passing through gaps between the drift tubes.

In addition, plots are made of the fraction of low Cherenkov photon production f. This fraction is defined as follows:

$$f = \frac{\text{number of tracks with less than 2 photons observed}}{\text{all tracks}} \tag{5.5}$$

The fraction f can help us identify bad sectors and/or runs. For example, threshold problems of the discriminator, low concentration of TMAE or misalignment, can cause a lower photon yield. By plotting the fraction f as a function of sector and run number, a good handle is obtained for the identification of bad sectors and runs. Figure 5.3 shows a plot of the fraction of low photon production taken from [11]. Bad periods or runs are discarded to ensure good quality of the analysed RICH data.

At this stage, we reject background in the RICH data. The major source of background is due to Cherenkov photons radiated in the liquid. For the minimum momentum we require in our analysis of τ decays that all particles traversing the liquid radiator produce the maximum number of Cherenkov photons, which is about 11. The photons enter the drift tube in the side facing the interaction region. The photons

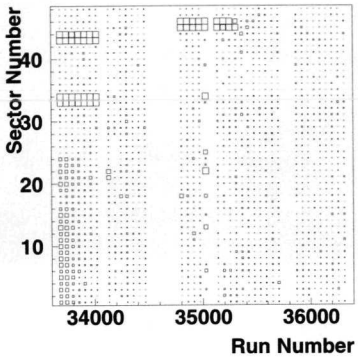

Figure 5.3: The fraction of low photon production as a function of sector number and run number. The surface of the squares is proportional to the value of the fraction.

emitted in the gas radiator are reflected in the mirrors and projected back onto the side of the drift tube facing outwards. The mean free path length for a Cherenkov photon in the drift tube is about 1.8 cm [12] (remember that the depth of the drift tube varies from 4.2 to 6.2 cm). The depth measurement of the MWPC's is used to kill the photons which have a high probability of coming from the liquid radiators. Secondly, we remove clusters of detected photons. Two photons belong to a cluster if they are found within a distance of 2.6 mm from each other. Clusters with more than 5 photons are rejected. Finally, there are Cherenkov photons producing hit-combinations of anode wires and cathode strips in the MWPC when they arrive at the same time. In such events, two photons are identified as four photons with equal drift time and hit pattern. The object is to determine which of the four photons are the two 'real' photons. To that extent, the Cherenkov angles are calculated for each photon, and the difference in Cherenkov angle is calculated for each pair. The photon pair with the largest difference in Cherenkov angle is rejected.

In di-muon events, deviations of the reconstructed Cherenkov angle from the saturated value signal an improper behaviour of the apparatus. For instance, in 1994 the index of refraction of the gasradiator was changed when the C_6F_{14} liquid leaked into the C_5F_{12} gas radiator. The C_6F_{14} is heavier than the C_5F_{12} and filled up the lower half of the detector. This way, the leakage of the liquid into the gas radiator showed up as a Cherenkov angle dependence on the azimuthal angle ϕ of the charged track.

The z-coordinate of the position where the Cherenkov photon is converted in the

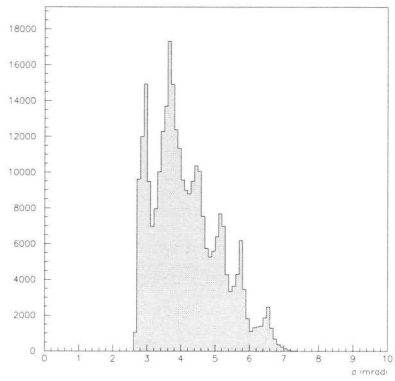

Figure 5.4: The error per photon on the measured Cherenkov angle for 1994 data.

drift tube, is calculated by measuring the drift time. Since the use of wrong values for the zero offset for the drift time and the drift velocity will lead to a shift of the Cherenkov ring, di-muon data are used to parameterize the residual z-shifts as a function of run number and drift distance. All calibration and alignment methods and results are described in detail in [11].

For each detected photon also the uncertainty of the measured Cherenkov angle is calculated. It contains contributions due to the bending of the track and the position resolution of the detection plane [11]. The uncertainty due to chromatic dispersion, i.e. the dependence of the index of refraction on the wavelength of a photon, is much smaller than the other error contributions and can be neglected. The total error is determined using the data from our di-muon sample to fit the resolution function:

$$F = \frac{\theta_\gamma - \theta_{exp}}{\sigma_\gamma} \tag{5.6}$$

where θ_γ and σ_γ are the Cherenkov angle per photon and its calculated error, and θ_{exp} is the expected Cherenkov angle, which is the 'saturated' value of 61.5 mrad for di-muon events. The error per photon is of the order of 2 to 7 mrad. The distributon of the error on the measured Cherenkov angle per photon for 1994 data is shown in figure 5.4. The six peaks in the distribution correspond to the six mirrors of the barrel RICH and are due to the contribution of the position resolution to the photon resolution. For a detailed study of the position resolution per mirror group, see [11].

The distribution of the photon resolution function, or pull, for di-muon events is shown in figures 5.5 through 5.8 for all years. The distribution is fitted with a Gaussian

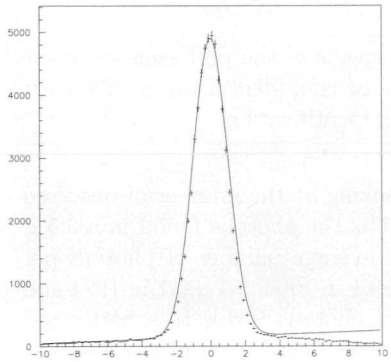

Figure 5.5: Pull for individual photons, 1992 di-muon data.

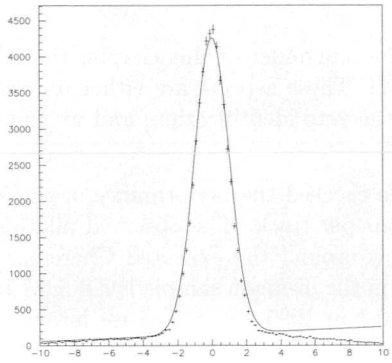

Figure 5.6: Pull for individual photons, 1993 di-muon data.

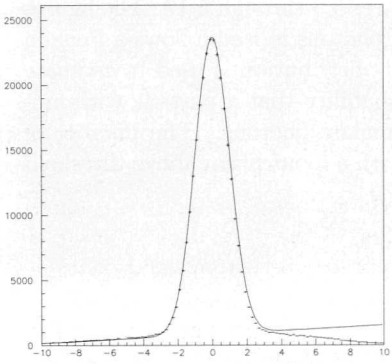

Figure 5.7: Pull for individual photons, 1994 di-muon data.

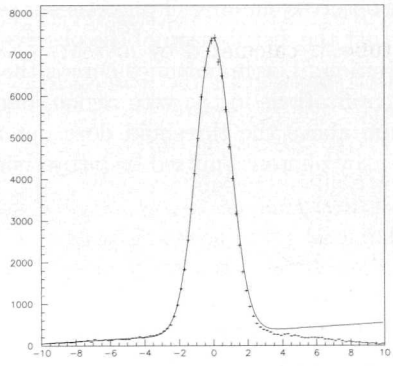

Figure 5.8: Pull for individual photons, 1995 di-muon data.

of width 1 and a linearly rising background[1]. The fit shows that the error we calculate for individual photons is well understood up to $+3\sigma$. Above $+3\sigma$, the fit shows disagreement. This is a feature of a cut made before the data is written on the DST. This cut rejects photons which are found further away than $+5\sigma_{DST}$, where σ_{DST} is the estimated error. The σ_{DST} however is found to be underestimated by a factor varying

[1]assuming a homogeneous background, the number of background photons increases with higher angles since the covered surface increases

from 1.2 to even 3.

The remainder of this chapter describes further aspects of the performance of the BRICH. These aspects are either important for veto- or ring identification. We start with the veto identification, and we end with the ring identification.

We checked the performance of the BRICH by looking at the number of observed photons per track. The observed photons are defined as the photons found in a 2.5 σ window around the expected Cherenkov angle. The average number of photons per track in the di-muon sample is 8.0 $\pm$0.1 in 1992, 8.3 $\pm$0.1 in 1993, 9.1 $\pm$0.1 in 1994 and 9.4 $\pm$0.1 in 1995. The increase in average number of photons is due to a better understanding and performance of the detector. In figures 5.9 through 5.12 the observed and expected number of photons for di-muons are shown for all years.

The expected number of photons differs per track. For each individual track it is used to generate a Poisson distribution. The thus obtained distribution is compared to the observed number of photons as is shown in figures 5.9 through 5.12. The figures show that the distribution of the observed number of photons indeed follows a Poisson distribution. The importance here is that the Poisson distribution is used to estimate misidentifications in the veto region, namely the probability that a particle with momentum above the threshold does not radiate Cherenkov photons. The number of Cherenkov photons emitted by a traversing particle with a momentum above threshold

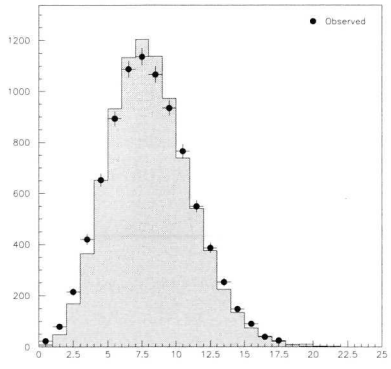

Figure 5.9: Observed and expected number of photons per track, 1992 di-muon data.

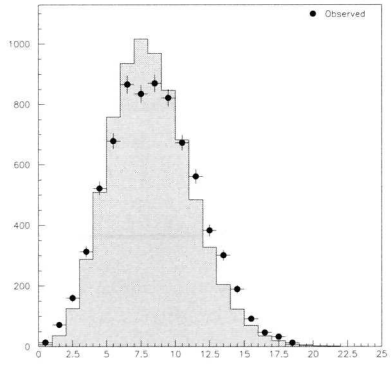

Figure 5.10: Observed and expected number of photons per track, 1993 di-muon data.

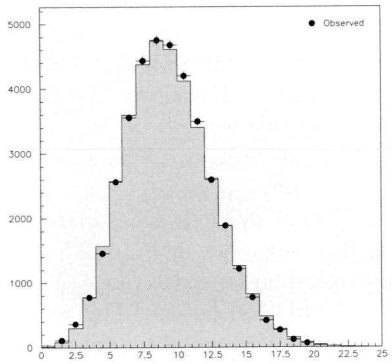

Figure 5.11: Observed and expected number of photons per track, 1994 di-muon data.

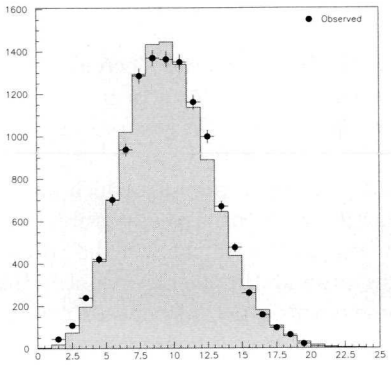

Figure 5.12: Observed and expected number of photons per track, 1995 di-muon data.

follows the Poisson distribution:

$$P(n) = a^n \frac{e^{-a}}{n!} \tag{5.7}$$

where a is the average number of Cherenkov photons, n the number of Cherenkov photons actually emitted (i.e. $< n >= a$) and $P(n)$ the probability of emitting n photons. The average number of photons depends on the mass and momentum of the particle, the distance traversed in the radiator and the photon detection efficiency of the RICH [13].

The misidentification rate in veto identification is defined as the probability P(0) to find no photons in a 2.5 σ window around the expected Cherenkov angle for a particle that does exceed the Cherenkov threshold. The analysis of di-muon events showed a variation in misidentification rate from 0.03 % (1992) to 0.008 % (1995).

We found that the veto identification is hampered by photons coming from the liquid radiator. Although we cut away many photons, which according to the depth measurement of the MWPC's come from the liquid, quite a number of photons can not be unambiguously attributed to either the liquid or gas radiator. In case the polar angle of the particle track is such that a portion of the liquid ring coincides with the (possible) gas ring, the detected photon can come from the liquid or the gas radiator. As a result, we can not distinguish between signal and background. We therefore cut away the polar angle region $\theta \in (70°, 110°)$ where liquid and gas rings overlap, for the

veto analysis. The analysis will be described in the next chapter.

Also to determine the Cherenkov angle per track for ring identification signal and background photons have to be distinguished from each other. To achieve this, the photons are grouped. A group is any subset of photons that could a priori be assigned to the track. We define good photons as the photons which are assigned to the group, the bad photons as photons which are excluded from the group.

Starting with the largest possible group, the average Cherenkov angle is calculated. Then, per photon we check if the corresponding Cherenkov angle lies within a 2.5 σ_γ window around the average value. Here, σ_γ is the single photon resolution. The outcome of this process leads to a new assignment of good and bad photons. This way, all permutations of the original set of photons are considered. If all good photons are found within the 2.5 σ_γ window and all bad photons outside this window, the set is called consistent. If only one consistent set is found, the average Cherenkov angle is the final Cherenkov angle for the track. If however, a second consistent set is found, the one with maximal number of photons and minimal variance in the photon angles of the set (with respect to the average angle) is chosen as the final Cherenkov angle. The difference in average Cherenkov angle of the two candidates is added in quadrature to the error.

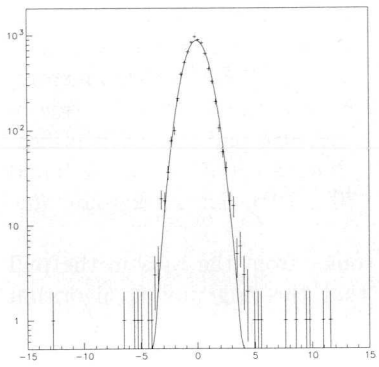

Figure 5.13: Pull for tracks, 1992 di-muon data.

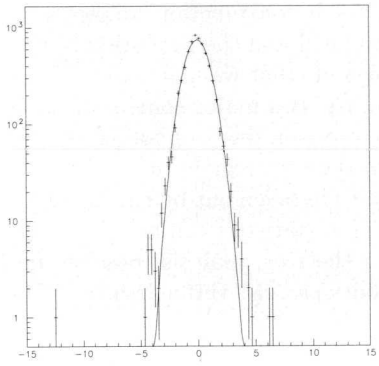

Figure 5.14: Pull for tracks, 1993 di-muon data.

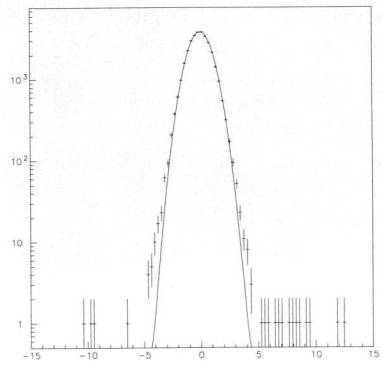

Figure 5.15: Pull for tracks, 1994 di-muon data.

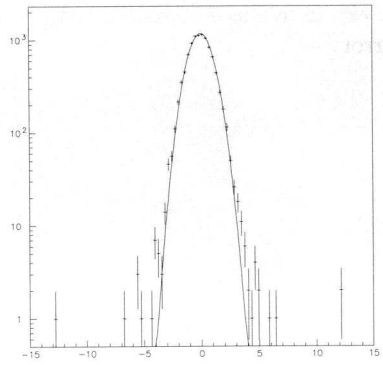

Figure 5.16: Pull for tracks, 1995 di-muon data.

In figures 5.13 through 5.16, the resolution function, or pull, for the average Cherenkov angle for di-muons is shown. The distribution is fitted with a Gaussian with width 1, centered around zero. The logarithmic scale shows that there are hardly any tails and thus no background, thus ensuring a low misidentification rate in the ring analysis. From the plots, we conclude that the measured Cherenkov angle agrees well with the expectation within the uncertainty of the measurement.

Summarizing, we conclude that the performance of the BRICH is good. The

Cherenkov photon yield follows the Poisson distribution nicely, and the Cherenkov angle resolution function follows a Gaussian with width 1. From the fact that the photon yield and the resolution of the BRICH are in agreement with our expectation, we conclude that we understand the performance of the BRICH. For the veto identification, the two major sources of background are understood: the misidentification in the veto region due to photons coming from the liquid radiator and the misidentification in the veto region due to Poisson statistics. The photons coming from the liquid radiator are taken out by cutting away the region $\theta \in (70°, 110°)$. The background due to Poisson statistics can be effectively estimated.

For the ring analysis, possible misidentification comes from the tails in the pull distributions 5.13 through 5.16. The figures show that the ring finding algorithm effectively suppresses the background. We are now ready to measure the very small fraction of kaons in single prong τ decays.

Chapter 6

Measurement of BR($\tau \rightarrow K\nu_\tau$)

In this chapter a number of τ decay channels are discussed. For a more complete overview of the τ decay modes we refer to appendix A. The branching ratio of the decay $\tau \rightarrow K\nu_\tau$ is measured using a sample of one prong τ decays. Only decays without particles interacting (mostly) electromagnetically (electrons, photons and π^0's) are selected. Ideally, this sample only contains the decays $\tau \rightarrow K\nu_\tau$, $\tau \rightarrow \pi\nu_\tau$ and $\tau \rightarrow \mu\nu_\mu\nu_\tau$. The branching ratio BR($\tau \rightarrow K\nu_\tau$) is then measured by determining the following ratio:

$$\mathcal{R}_{meas} = \frac{\text{number of } \tau \rightarrow K\nu_\tau}{\text{number of } \tau \rightarrow \pi\nu_\tau \text{ or } \mu\nu_\tau\nu_\mu} \tag{6.1}$$

If ε_i , $i = K, \mu, \pi$ are the efficiencies with which we select and identify the decay channels, the following equation is valid:

$$\mathcal{R}_{meas} = \frac{\varepsilon_K BR(\tau \longrightarrow K\nu_\tau)}{\varepsilon_\mu BR(\tau \longrightarrow \mu\nu_\tau\nu_\mu) + \varepsilon_\pi BR(\tau \longrightarrow \pi\nu_\tau)} \tag{6.2}$$

A KORALZ [7] generated $Z^0 \rightarrow \tau^+\tau^-$ event sample with full detector simulation [1] is used to obtain the factors ε_i. The total simulated event sample corresponds to almost four times the integrated luminosity taken by DELPHI in 1994. The branching ratio $\tau \rightarrow K\nu_\tau$ is obtained through

$$BR(\tau \rightarrow K\nu_\tau) = \mathcal{R}_{meas} \times \left(\frac{\varepsilon_\mu}{\varepsilon_K} BR(\tau \rightarrow \mu\nu_\tau\nu_\mu) + \frac{\varepsilon_\pi}{\varepsilon_K} BR(\tau \rightarrow \pi\nu_\tau) \right) \tag{6.3}$$

6.1 Event selection

We used the data recorded at DELPHI in the years 1992, 1993, 1994 and 1995. The total hadronic event sample for these years amounts to 751 k Z^0's in 1992, 755 k Z^0's in 1993, 1484 k Z^0's in 1994 and 750 k Z^0's in 1995 [5].

[1] The RICH detector was not included in the detector simulation

To select single prong τ decays, the event is divided into two hemispheres. First, the thrust axis is calculated using the charged particles. These particles have to have a momentum of at least 0.6 GeV. Furthermore, the tracks have to come from the interaction point to within 4.5 cm in z and 0.2 cm in the xy-plane. For the distance in xy applies that if there are no vertex detector hits on the track, this distance is 4.0 cm. The small value (i.e. 0.2 cm) is chosen in order to reject photo conversions and cosmics. The event is then divided by a plane perpendicular to the thrust axis. One side is constrained to contain only one charged particle whereas the other side can contain up to three charged particles.

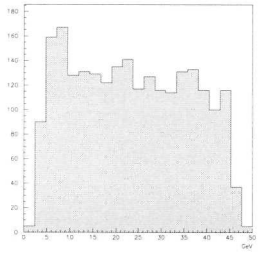

Figure 6.1: Kaon momentum distribution

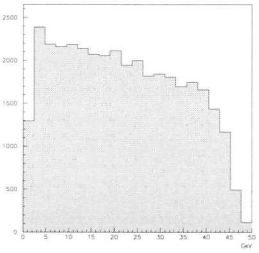

Figure 6.2: Pion momentum distribution

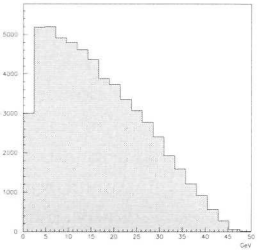

Figure 6.3: Muon momentum distribution

Next, kinematical constraints are applied only to sides with one charged track to allow particle identification in the RICH. The track has to pass through the barrel RICH and therefore, the polar angle of the track has to be between 47° and 133°. The momentum of the single charged track has to be higher than 4 GeV and lower than 25 GeV. The lower limit is set to 4 GeV to ensure the yield of a maximal number of Cherenkov photons for pions and muons. This leads to less background in the kaon veto identification. Since kaons are produced in τ decays with a minimal momentum of 3.5 GeV, we do not lose many kaons with this cut, see figures 6.1 through 6.3. At 25 GeV, kaons have an almost saturated Cherenkov angle and separation between kaon and π is no longer possible.

Now, the sample we are left with is already quite pure in τ decays. The Bhabha and di-muon events are rejected by the requirement that charged tracks have to have a momentum of maximally 25 GeV. The minimum momentum of 4 GeV rejects a large fraction of two-photon events. The constraint of only one charged particle on at least one side rejects hadronic events. We note, that the cuts we described until now, are the kinematical requirements for kaon identification in the RICH.

The background is further reduced by a cut on the angle between the charged track on the one-prong side and the closest charged track in the opposite hemisphere, which

has to be larger than 165°. Then, a cut on the opposite side is introduced. In order to suppress non-Z^0 background, the scalar sum of the charged particle momenta in the opposite hemisphere has to be more than 1 GeV.

For a determination of the branching ratio $BR(\tau \to K\nu_\tau)$, we have to distinguish between kaons and K^*'s. For this purpose, a set of cuts based on the measurements of the electromagnetic calorimeter (HPC) is introduced. The cuts are designed to reject any τ decay which includes those particles interacting mostly electromagnetically. As a consequence, the decay $\tau \to e\nu_e\nu_\tau$ will be rejected too by these cuts. The rejection of the electron channel is only to our advantage since the RICH misidentification rate is expected to be much higher for electrons than for muons or pions (see section 4.2). Because there is no need to distinguish between electrons or decays which include neutral(s), the cuts described below are much easier to implement and are more efficient than the cuts described in chapter 4. The electron tag which is explained in chapter 4 is developed for the determination of the K^* branching ratio, the determination of which will not be presented in this thesis.

We note that kaons and π's can produce hadronic showers in the HPC. Those showers start typically late in the HPC, they are broader and show larger statistical fluctuations than electromagnetically induced showers. The hadronic showers should not be rejected by our cuts. With the following set of cuts, τ decays which include electromagnetically interacting particles are identified:

- The ratio of the total electromagnetic energy deposited in a 20° cone around the thrust axis and the momentum is higher than 0.7. If the charged track traverses θ-cracks or ϕ-cracks in the HPC, this value is set to 0.45 and 0.2 respectively.

- The total neutral electromagnetic energy (i.e. not connected to the charged track) in the 20° cone is more than 0.4 GeV. The contributions from different showers are weighted with the distance to the track. The weight only applies to showers close to the charged track.

- There is an additional (rejected) track in the hemisphere. Usually this track comes from a photon conversion.

Cosmic events can lead to a mismeasurement of the branching ratio $BR(\tau \to K\nu_\tau)$. A cosmic track going through the interaction point will radiate Cherenkov photons away from the mirror system in the upper half of the detector, whereas in the lower half of the detector it will be detected by the RICH. If the momentum of the cosmic track is in the momentum region for kaon veto identification, the event will look like a perfectly normal $e^+e^- \to \tau^+\tau^-$ event where one τ decays to a μ (lower half of the detector) and the other τ decays to a kaon. The event sample we selected still contains cosmics. The cosmic events are identified with an appropriate set of cuts of which the most important are the requirement of collinear tracks (the a-collinearity had to be less than 2.5°) and the constraint that the momenta of the charged tracks are equal within 5σ. Once identified, the cosmic events were rejected.

τ decay	Original sample composition	Efficiency all cuts except HPC cuts	Efficiency all cuts	Sample composition
e	$17.73 \pm 0.06\%$	$24.38 \pm 0.17\%$	$0.30 \pm 0.02\%$	$0.63 \pm 0.05\%$
μ	$17.98 \pm 0.06\%$	$33.67 \pm 0.18\%$	$32.24 \pm 0.18\%$	$67.79 \pm 0.26\%$
π	$11.38 \pm 0.05\%$	$23.11 \pm 0.21\%$	$18.78 \pm 0.19\%$	$24.99 \pm 0.24\%$
ρ	$24.67 \pm 0.07\%$	$31.35 \pm 0.15\%$	$1.07 \pm 0.03\%$	$3.09 \pm 0.10\%$
a_1	$8.45 \pm 0.05\%$	$33.70 \pm 0.27\%$	$0.08 \pm 0.02\%$	$0.08 \pm 0.02\%$
K	$0.72 \pm 0.01\%$	$23.09 \pm 0.82\%$	$19.38 \pm 0.77\%$	$1.63 \pm 0.07\%$
K^*	$0.42 \pm 0.01\%$	$36.25 \pm 1.22\%$	$1.56 \pm 0.32\%$	$0.08 \pm 0.02\%$

Table 6.1: The sample composition of the original sample, the efficiency of the set of all cuts except the HPC cuts, the efficiency of the consecutive appliance of the HPC cuts, and the resulting sample composition after all cuts have been applied. The data is obtained through the KORALZ τ generator with full detector simulation.

By applying all cuts, we select the channels which enter the ratio (6.1). The background cuts include cuts on the momentum, cosmics, the sum of the charged momentum on the second hemisphere and the isolation angle cut. The track quality cuts include the constraint of having track elements in both the TPC and the Outer detector. The HPC cuts include the cuts described previously. In table 6.1 the effect of the set of HPC cuts on the event sample is given. The table shows the relative abundancy of the three decay channels μ, π and K which pass the HPC cuts. Also clear is that the selection efficiencies for π and K are equal. In principle the μ efficiency should be equal too, but the momentum spectrum of the μ is slowly decreasing (see figure 6.3), leading to a relative abundancy of μ with respect to π and K. The abundancy of K^* before the HPC cuts is due to the fact that $\tau \rightarrow K^*\nu \rightarrow K\pi\nu$ is a three-body decay, causing the momentum spectrum of the final state particles to be softer.

There is still some background to be expected. For events with multiple charged tracks in either hemisphere, the background is due to hadronic Z^0 decays. For events which have a 1-1 topology (one charged track per hemisphere), the background comes from Bhabha, di-muon events, two-photon events and cosmics.

The selected sample is therefore checked for those variables which are particularly

Charged multiplicity in other hemisphere	Data	KORALZ	Difference
one	$81.0 \pm 0.5\%$	$80.8 \pm 0.2\%$	$0.3 \pm 0.5\%$
two	$3.9 \pm 0.2\%$	$4.1 \pm 0.1\%$	$-0.2 \pm 0.2\%$
three	$14.2 \pm 0.4\%$	$14.0 \pm 0.2\%$	$0.2 \pm 0.5\%$
more than three	$0.9 \pm 0.1\%$	$1.1 \pm 0.1\%$	$-0.2 \pm 0.1\%$

Table 6.2: Percentages of the number of charged tracks on the opposite hemisphere in 1994 data and in τ KORALZ simulated events.

sensitive to background. First of all, the performance of the HPC cuts is studied in detail on simulated data: KORALZ generated $e^+e^- \rightarrow \tau^+\tau^-$ events with full detector simulation. In real data, most background will come from Bhabha events and hadronic events. If these events are present in the selected sample, one expects to find more photons coming from the Bhabha's, and more π^0's coming from hadronic events. Therefore, the fraction of events rejected by the HPC cuts is a sensitive indication for the existence of background.

A comparison was made between real data and KORALZ simulated data concerning the fraction of events which passed the HPC cuts. For KORALZ simulated data $34.3 \pm 0.2\%$ of the tracks passed the HPC cuts. For real data this fraction is $33.3 \pm 0.4\%$. We thus see that KORALZ simulated data and real data agree within the order of 1 %. Since the HPC cuts cut away neutrals and electrons, and, the percentages of all data events and τ KORALZ events killed by the HPC cuts agree, we conclude that our set of cuts prior to the HPC cuts, effectively reject Bhabha and hadronic events.

Since most cuts described in this chapter apply to the one prong hemisphere, the second side is relatively unbiased. Therefore, the charged multiplicity on the second side is a sensitive indication for possible background. Again, the expectation is that the presence of Bhabha and hadronic events alter the fractions of 1-1, 1-2, 1-3 and 1-n (n=4,5,6) topologies. In table 6.2 the percentages of one, two, three or more than three charged tracks on the second side are given for data and KORALZ. The comparison shows that we understand our sample composition to within 1 %.

6.2 Kaon identification with the RICH

The sample we obtained after applying all cuts consists mainly of the three τ decay channels as given in equation 6.2. All particle momenta are between 4 and 25 GeV and all particles traverse the barrel region ($\theta \in 47° - 133°$). In DELPHI we can distinguish the $\tau \rightarrow K\nu_\tau$ channel from the μ/π channel on a track-by-track basis using the particle identification of the RICH detector. Dictated by the momentum range of the particles, only the RICH gas radiator is used in the analysis. We will make a two-fold separation in our sample: the particles will either belong to the kaon-class or to the μ/π-class. In other words, we will not attempt to distinguish μ's from π's. Before we can identify particles, the sample is further cleaned from background to provide reliable RICH identification.

Two identification methods are used. Kaons start radiating Cherenkov photons at 9 GeV (chapter 5). From 4 to 9 GeV kaons traverse the gas radiator without emitting Cherenkov photons. For μ's and π's, this threshold is already passed before 4 GeV. Therefore, in between 4 and 9 GeV, distinction can be made between kaons and μ's/π's, by the absence or presence of photons in a $2.5\sigma_\gamma$ window around $\theta_{(\pi/\mu)}$. The angle $\theta_{(\pi/\mu)}$ is the saturated Cherenkov angle in the gas radiator, corresponding to 61.5 mrad. As mentioned before, the method of distinguishing particles by the absence of photons is called veto identification.

Above 9 GeV particles are identified by measuring the Cherenkov angle. The measured angle is compared to the expected Cherenkov angle for the different particle

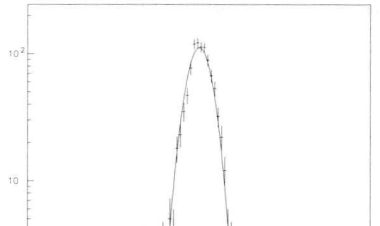

Figure 6.4: Pull per track for τ one prong ring identification selection for 1992 data.

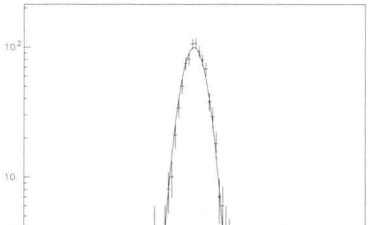

Figure 6.5: Pull per track for τ one prong ring identification selection for 1993 data.

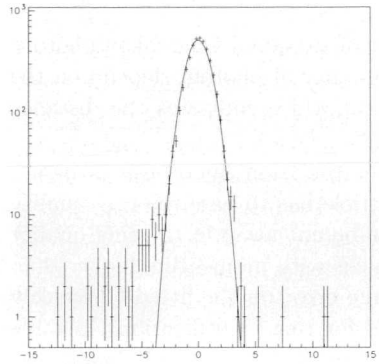

Figure 6.6: Pull per track for τ one prong ring identification selection for 1994 data.

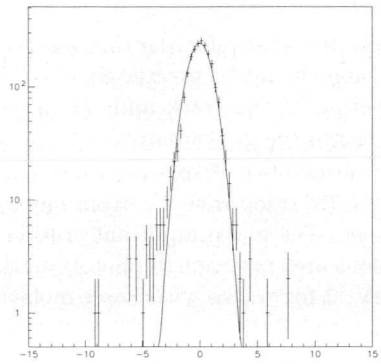

Figure 6.7: Pull per track for τ one prong ring identification selection for 1995 data.

hypotheses and the particle is then attributed to one of the two classes (i.e. the kaon class or the π/μ class). This is called, as mentioned previously, ring identification. Through the iterative procedure discussed in section 5.3 the average Cherenkov angle is determined. In figures 6.4 through 6.7 the pull distributions for our one prong τ sample are given for all years. In the plots a Gaussian with width 1 is drawn. The pull distributions of the one prong τ sample agree well with the pull distributions of the di-muon sample studied in chapter 5.

The pull is made with respect to the pion hypothesis. The 'shoulder' on the left hand sides of the distributions indicate the presence of kaons. The logarithmic plots show that there is almost no background.

In order to ensure a reliable RICH identification, the particles have to pass the RICH quality cuts as described in the di-muon study in the previous chapter; particles without hits in the TPC and OD are discarded. Bad runs and bad sectors are cut away, and particles without dE/dX hits in the RICH are discarded. Tracks with no or inconsistent RICH data are discarded and tracks with too high background (more than 30 photons connected to the track) are cut. After this general RICH quality selection, there is another, identification method dependent, quality selection. This will be discussed in sections 6.3 and 6.4.

After applying all event selection cuts and all RICH quality cuts, we selected a total sample of 1788 one prong τ decays in 1992, 1698 in 1993, 7721 in 1994 and 3826 one prong τ decays in 1995.

6.3 Ring identification

In order to classify for the ring analysis, the number of expected Cherenkov photons for a kaon should be greater than 2. The expected number of photons depend on the momentum of the track and the angle θ of the track, which indicates the distance traversed in the gas radiator.

If the number of expected Cherenkov photons for the kaon hypothesis is higher than 2 for a track with a certain momentum, the particle has to pass the ring quality selection. The most important criteria for a track to be cut away in the ring quality selections are: not enough photons in the fit (3 for tracks with momentum higher than 15 GeV, 2 for tracks with lower momentum), too large error on the fitted Cherenkov angle, a bad RMS on the fit, or too high background for ring identification. In table 6.3 numbers are given for tracks which passed these cuts. The term 'good conditions' hereby refers to passing the above mentioned ring quality cuts.

For each detected photon, the angle with respect to the particle's trajectory, and its error are calculated [11],[13]. The Cherenkov angle of the particle is determined through the iterative procedure as described in section 5.3. A particle is tagged as a kaon if the Cherenkov angle is in agreement with the kaon hypothesis, i.e. if the angle is found within a 2.5 σ window around the expected Cherenkov angle for a kaon with similar momentum, *and incompatible* with the π/μ hypothesis. The latter constraint being more than 3.3 σ below the expected angle for μ/π. The value of 3.3 was carefully

Year	1992	1993	1994	1995
Enter the analysis	1788	1698	7721	3826
Of which have more than 2 expected photons in the K hypothesis	1273	1150	5640	2753
Of which good conditions	989	875	4461	2140
Of which:				
Tagged as Kaon	11	10	65	25
Tagged as Pion/Muon	545	493	2574	1213

Table 6.3: Results from the ring analysis for all years

chosen after varying it over a wide range. The parameter indicating the value is called SEP in this analysis. Its influence on the result is discussed in more detail in section 6.5.

As the particle momentum increases, the acceptance for kaon identification becomes less and less because the kaon ring starts to overlap with the (saturated) μ/π ring. The acceptance for particle identification as a function of momentum is given in section 6.5. Table 6.3 gives a listing of the number of particles during the various stages of the ring identification analysis for all years. The last two lines of the table give the identified kaons and pions. This amounts to a bit over 30 % of the tracks which enter the analysis. Those tracks which can not be identified either have too low momentum to have the required two photons in the kaon hypothesis, do not fullfill the ring quality constraints, or have too high momentum such that the kaon band and the pion band overlap (in which case no distinction can be made).

Looking at the one prong τ selection for ring identification, we find that the average number of Cherenkov photons per track in our τ selection is 7.9 $\pm$0.2 for 1992, 8.3 $\pm$0.3 for 1993, 9.0 $\pm$0.1 for 1994 and 9.3 $\pm$0.1 for 1995. The averages are obtained with a data sample which passed the general RICH quality cuts and the constraints for good ring conditions. The distributions of the number of photons per track for all years are given in figures 6.8 through 6.11. They are in agreement with the results obtained from the di-muon sample (figures 5.9 through 5.12).

6.4 Veto identification

Particles qualify for the veto analysis if the number of expected Cherenkov photons in the kaon hypothesis is less than 3. If a particle satisfies this constraint, it has to pass the veto quality cuts. The veto quality cuts include too low number of expected pion photons, no dE/dx hits in the RICH and too high background (more than 2 photons in a 2.5 - 5 σ window around the pion Cherenkov angle). Since kaons are identified by

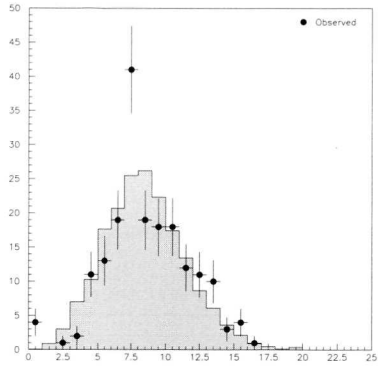

Figure 6.8: Number of observed and expected photons for 1992 data.

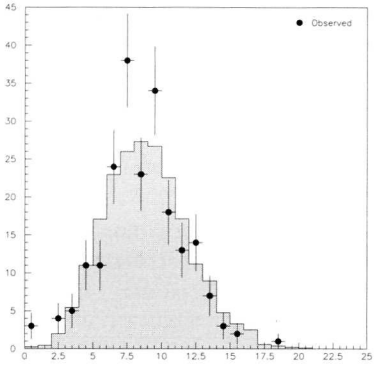

Figure 6.9: Number of observed and expected photons for 1993 data.

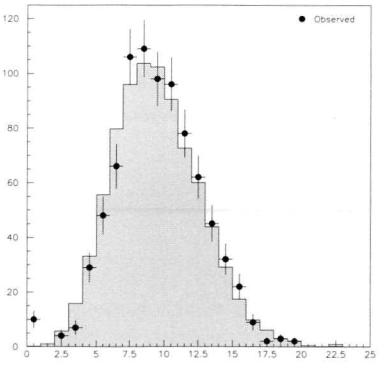

Figure 6.10: Number of observed and expected photons for 1994 data.

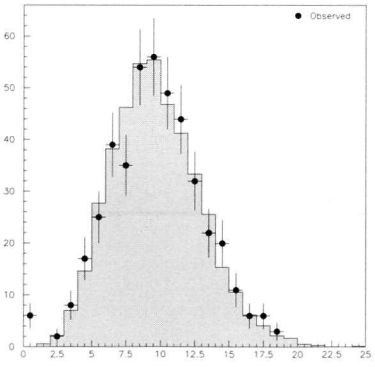

Figure 6.11: Number of observed and expected photons for 1995 data.

the absence of photons in the band around the expected Cherenkov angle for μ/π, we also cut out the region $\theta \in (70°, 110°)$ from our veto identification analysis to avoid overlapping liquid and gas rings. With this cut, about one-third of the tracks are rejected.

In figures 6.8 through 6.11 the observed and expected number of photons for our one prong τ selection for veto identification are shown. The expected number of Cherenkov photons is calculated under the assumption that the particle is a pion. The excess in the zero bin is due to the presence of kaons in the sample.

Year	1992	1993	1994	1995
Enter the analysis	1788	1698	7721	3826
Of which have less than 3 expected photons in the K hypothesis	515	548	2081	1073
Of which good conditions	187	211	829	435
Of which:				
Tagged as Kaon	4	3	10	6
Tagged as Pion/Muon	183	208	819	429

Table 6.4: Results from the veto analysis for all years

We end this section with an overview of the amounts of particles during the various stages of the veto analysis. The overview is given in table 6.4.

6.5 The branching ratio $\mathbf{BR}(\tau \to K\nu_\tau)$

In the beginning of this chapter the branching ratio calculation was given by equation 6.3. In fact, this is the ideal situation. What we really measure as kaon sample is given in the following equation:

$$\begin{aligned} N_{K,identified} &= (\varepsilon_K BR(\tau \to K\nu_\tau) + \varepsilon_{K^*} BR(\tau \to K^*\nu_\tau) + \\ &\quad \delta_\pi BR(\tau \to \pi\nu_\tau) + \delta_\mu BR(\tau \to \mu\nu_\mu\nu_\tau)) \times N_\tau \end{aligned} \tag{6.4}$$

Here, δ_π and δ_μ are the probabilities to select pions that do not radiate any photons (for veto), or the probabilities that the average Cherenkov angle for the pion and the muon satisfies the SEP constraints to be tagged as a kaon (for ring). ε_K and ε_{K^*} are the efficiencies to select K's and K^*'s, the latter being selected because the HPC cuts did not keep all the K^*'s out of our sample.

The correct formula with which the branching ratio is calculated thus reads:

$$\begin{aligned} BR(\tau \to K\nu_\tau) &= \mathcal{R}_{meas} \times \\ &\quad \left(\frac{\varepsilon_\mu}{\varepsilon_K} BR(\tau \to \mu\nu_\tau\nu_\mu) + \frac{\varepsilon_\pi}{\varepsilon_K} BR(\tau \to \pi\nu_\tau) + \right. \\ &\quad \left. \frac{\varepsilon_\rho}{\varepsilon_K} BR(\tau \to \rho\nu_\tau) + \frac{\varepsilon_{a_1}}{\varepsilon_K} BR(\tau \to a_1\nu_\tau)\right) - \\ &\quad \frac{\varepsilon_{K^*}}{\varepsilon_K} BR(\tau \to K^*\nu_\tau) - \frac{\delta_\pi}{\varepsilon_K} BR(\tau \to \pi\nu_\tau) - \\ &\quad \frac{\delta_\mu}{\varepsilon_K} BR(\tau \to \mu\nu_\mu\nu_\tau) \end{aligned} \tag{6.5}$$

Here, $\mathcal{R}_{meas}$ is the ratio of the number of kaons we identify and measure, and the number of pions/muons we identify and measure.

The efficiencies used in equation 6.5 are obtained as follows. The choice between using the veto identification method or the ring identification method is dictated by the momentum and the polar angle of the particle. Because of the dependence on the polar angle, the momentum regions for veto identified particles and ring identified particles overlap. This is shown is figures 6.12 through 6.14.

The figures 6.12 through 6.14 are obtained from 1994 data. The efficiency is calculated with the one-prong τ sample where the tracks passed all cuts except the RICH related cuts. By dividing the identified tracks by the total sample the efficiency is determined. The relatively low identification efficiency in the veto region is due to the $\theta \in (70°, 110°)$ cut. The decrease of ring efficiency with increasing momentum is caused by the increasing overlap of kaon and pion rings. The RICH identification efficiency for 1994 data as shown in figure 6.14 is then combined with the Monte Carlo simulation to determine the overall efficiency for specific one prong τ decay channels. We used figure 6.14 to weight every particle with the efficiency of the bin which corresponds with the

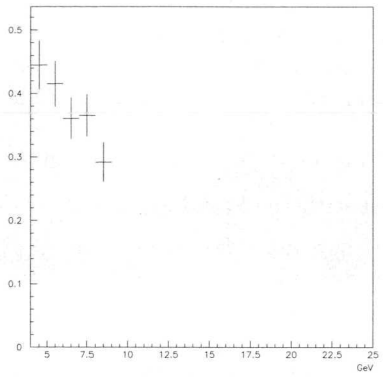

Figure 6.12: Veto identification efficiency for 1994 data.

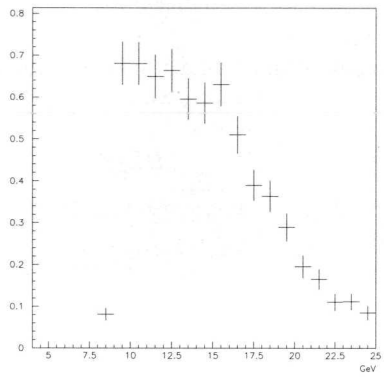

Figure 6.13: Ring identification efficiency for 1994 data.

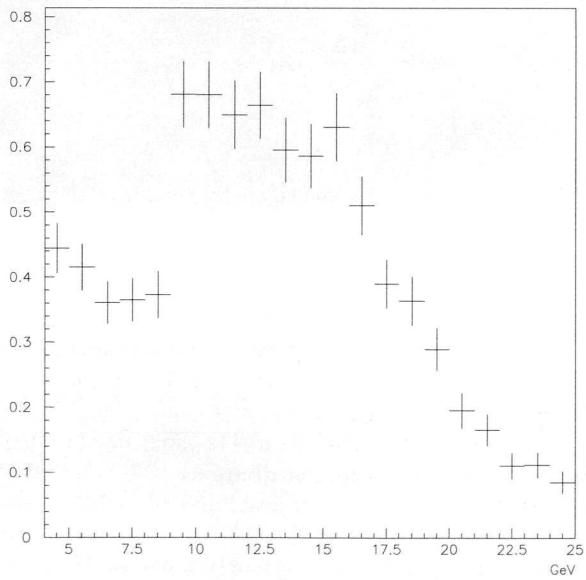

Figure 6.14: Total identification efficiency for 1994 data.

momentum of the particle. This way, the momentum dependence of the RICH particle identification is taken into account in the final selection efficiencies ε_i's as well as the effect of the RICH quality cuts.

Table 6.5 shows that the branching ratios $\tau \rightarrow K\nu_\tau$ for all years agree. The overall result for the branching ratio $\tau \rightarrow K\nu_\tau$ is found by taking the weighted average of all years:

$$BR(\tau \rightarrow K\nu_\tau) = 0.775 \pm 0.074_{stat}\% \tag{6.6}$$

The result given in equation 6.6 is in good agreement with the Standard Model prediction:

$$BR(\tau \rightarrow K\nu_\tau) = 0.72 \pm 0.01\% \tag{6.7}$$

The δ_π and δ_μ are connected with particle misidentification. Particle misidentification was corrected for on a statistical basis. In table 6.5 the identified kaons and pions are listed together with misidentified particles. The first kind of misidentification impacts the veto identification result. The probability for a particle above threshold not to radiate any photons is calculated through the relevant Poisson distribution. For every track, the probability P(0) (see equation 5.7) was calculated and summed.

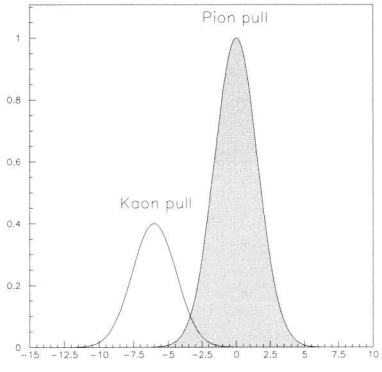

Figure 6.15: Example of overlapping pull distributions.

The second type of misidentification impacts the ring identification result. Depending on the momentum of the particle, the pull distributions of the kaon and the pion overlap (see figure 6.15). This leads to the possibility that a pion can have a Cherenkov angle incompatible with the pion hypothesis, and compatible with the kaon hypothesis. In order to calculate the number of misidentified pions, the part of the pion pull

compatible with the kaon hypothesis, was integrated and summed for every track. The contribution of δ_π and δ_μ to the systematical error is in both cases (i.e. in veto and ring identification) negligible.

In table 6.6 a listing is given of all variables which contribute to the systematical error. For all variables the uncertainty is known, either by calculation (statistical error on the ε's) or taken from the Particle Data Group (branching ratios) [14]. All contributions to the systematic error were obtained by varying the corresponding variable by $\pm 1\sigma$ and monitoring the change in the branching ratio result. None of the variables showed an asymmetric contribution to the systematical error.

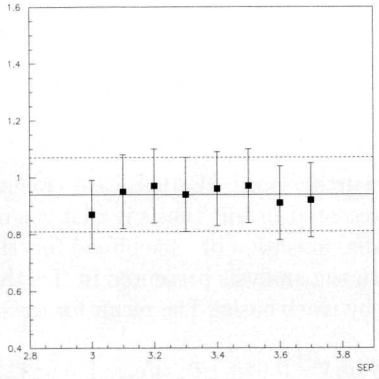

Figure 6.16: Ring branching ratios as a function of SEP for 1994 data. The horizontal lines indicate the ring branching ratio and the uncertainty on it for 1994 data.

Besides the uncertainty on ε_i's, there are still two important contributions to the systematic error. They are the uncertainty on the branching ratios taken from the particle data booklet and the contribution due to the parameter SEP, which is used to distinguish kaons from pions/muons in the ring identification method (see section 6.3). SEP was varied over a wide range of values. By increasing SEP the background decreases and the number of identified particles (acceptance) becomes lower. The branching ratio $\tau \rightarrow K\nu_\tau$ is stable for SEP above the value 3 as shown in figure 6.16. The contribution to the systematic error due to the acceptance, SEP, is as well specified in table 6.6.

Together with the efficiency to select K's (ε_K), SEP forms the leading contribution to the systematic error. The ε_K because it is directly coupled to the branching ratio $BR(\tau \rightarrow K\nu_\tau)$ and therefore forms the denominator for all terms on the right-hand side of equation 6.5. SEP because this variable determines if a particle is a K or a π/μ

in the RICH identification algorithm.

The total systematical error is obtained by adding up the squared separate contributions.

With all systematics taken into account, the overall result for the branching ratio $\tau \rightarrow K\nu_\tau$ is:

$$BR(\tau \rightarrow K\nu_\tau) = 0.775 \pm 0.074_{stat} \pm 0.055_{sys}\% \tag{6.8}$$

In September 1998 the fifth international workshop on τ lepton physics was held in Santander, Spain. There, results were shown from other groups or experiments. The main two contributions on single prong kaon production in τ decays came from the DELPHI and ALEPH experiments at CERN. The DELPHI analysis was later updated for the HEP'99 conference in Finland [15].

For DELPHI the data analysed was taken from the years 1993 through 1995. The ALEPH collaboration analysed the data taken in 1991 through 1995. The DELPHI analysis was, just as in the analysis presented in this thesis, based upon the particle identification with the RICH. Furthermore, dE/dx measurements were used. The main difference with the analysis presented in this thesis is that the other DELPHI analysis obtained the result through a maximisation of a likelihood function of dE/dx and RICH pulls [15]. This in contrast with the analysis presented in this thesis where we uniquely identifiied particles on a track by track basis. The result for the other DELPHI analysis is:

$$BR(\tau \rightarrow K\nu_\tau) = 0.648 \pm 0.045_{stat} \pm 0.043_{sys}\% \tag{6.9}$$

This result is, within 1 σ, in agreement with the result presented in this thesis. The reason why both DELPHI analyses differ in result using the same data set is because completely different event selections are used, i.e. the standard DELPHI τ selection versus the RICH identification based event selection presented in this thesis. On top of that, the methods of determining the kaon contents in the data samples differs completely.

ALEPH presented a preliminary result, which was later published [16]. The ALEPH analysis is solely based on their excellent dE/dx measurements. Their result reads:

$$BR(\tau \rightarrow K\nu_\tau) = 0.696 \pm 0.025_{stat} \pm 0.014_{sys}\% \tag{6.10}$$

The remarkable difference in statistical error is mostly due to the fact that the ALEPH detector covers a larger solid angle and a larger K momentum interval is used in the dE/dx measurement.

In february 2001, OPAL published their result on one-prong τ decays with a charged kaon [17]. The results were obtained using the complete set of data collected by the

OPAL experiment between 1990 and 1995. The branching ratio for the exclusive τ to kaon decay reads:

$$BR(\tau \rightarrow K\nu_\tau) = 0.658 \pm 0.027_{stat} \pm 0.029_{sys}\% \tag{6.11}$$

Again, the results were obtained from an analysis of the ionisation energy loss of charged particles selected from $e^+e^- \rightarrow \tau^+\tau$ candidates.

All results are in good agreement.

6.6 Conclusion

We measured the exclusive kaon production in one prong τ decays $\tau \rightarrow K\nu_\tau$ using the data collected by the DELPHI detector in 1992, 1993, 1994 and 1995.

Two identification methods based on the measurements of the RICH detector are used to obtain the total number of kaons produced. The methods are described in the previous sections, the results from the different methods are given in table 6.5.

The branching ratio BR($\tau \rightarrow K\nu_\tau$) is calculated using the Standard Model. In the Standard Model, all leptons couple to the W boson with universal strength. Our measurement is in agreement with the Standard Model prediction and thereby we indirectly confirm lepton universality.

The combination of the low branching ratio BR($\tau \rightarrow K\nu_\tau$) and the precise theoretical prediction makes the measurement of this decay a sensitive instrument for interactions beyond the Standard Model. Our branching ratio measurement does not indicate the existence of interactions beyond the Standard Model. With two standard deviations or 95 % confidence level, we set limits on possible new interaction couplings. First, the branching ratio is determined as described in the previous section. Then, limits can be set on the different additional couplings through relations (2.18) to (2.20). This results in relations for additional interaction couplings as given in table 6.7.

The g'_i's are the additional interaction couplings as defined in appendix B. We note that the g''s indicate the fraction of the Standard Model coupling. This means that if we assume $g'_\mu \simeq 0$, the combination $g'_{us}g'_\tau$ should be less than 4 % of the combination of Standard Model couplings in case of a V-A Lorentz structure (first line of table 6.7).

Year	1992	1993	1994	1995
Ring good conditions	989	875	4461	2140
Ring kaons	11	10	65	25
Ring fraction K^*	0.80	0.72	3.70	1.77
Ring misidentified pions/muons	0.54	0.55	2.14	1.12
Ring pions/muons	545	493	2574	1213
Ring branching ratio	0.729 ± 0.245	0.728 ± 0.257	0.943 ± 0.127	0.749 ± 0.166
Veto good conditions	187	211	829	435
Veto kaons	4	3	10	6
Veto fraction K^*	0.12	0.13	0.53	0.28
Veto misidentified pions/muons	0.10	0.07	0.19	0.08
Veto pions/muons	183	208	819	429
Veto branching ratio	1.006 ± 0.530	0.653 ± 0.402	0.552 ± 0.187	0.641 ± 0.277
Total branching ratio	0.778 ± 0.222	0.706 ± 0.217	0.819 ± 0.105	0.721 ± 0.143

Table 6.5: The combined result for veto and ring identification analysis per year. Apart from the branching ratios, all numbers indicate number of events. The branching ratios only give statistical errors.

Parameter	Value and sigma %	Contribution %
ε_K	ring 7.22 ± 0.50 veto 1.45 ± 0.23	0.047
ε_μ	ring 11.93 ± 0.13 veto 3.02 ± 0.07	0.005
ε_π	ring 7.04 ± 0.12 veto 1.39 ± 0.06	0.003
ε_ρ	ring 0.41 ± 0.02 veto 0.08 ± 0.01	0.001
ε_{K^*}	ring 0.77 ± 0.22 veto 0.08 ± 0.01	0.012
$BR(\tau \rightarrow \mu)$	17.37 ± 0.09	0.003
$BR(\tau \rightarrow \pi)$	11.08 ± 0.13	0.003
$BR(\tau \rightarrow K^*)$	0.52 ± 0.05	0.005
SEP	3.0 ± 0.3	0.025
total		0.055

Table 6.6: The contributions to the systematical error. Parameters which do not show up in this table have a negligible contribution

Lorentz structure	Limit
V-A	$g'_{us}(g'_\tau - g'_\mu) < 0.039$
V+A	$g'^2_{us}(g'^2_\tau - g'^2_\mu) < 0.017$
V or A	$g'_{us}(g'_\tau - g'_\mu) < 0.077$

Table 6.7: Limits on additional interaction couplings for several Lorentz structures with 95 % confidence level. Only the uncertainty on the measured branching ratio $BR(\tau \rightarrow K\nu_\tau)$ is taken into account

Appendix A

Resonances in τ decays

In this appendix relative contributions of final state decay channels of τ decays to resonances, are given. The resonances taken into account in this note are ρ, K^*, a_1, K_1 and $\rho(1700)$. To determine the relative contributions of different final state channels, use is made of Clebsch Gordan coefficients for isospin decomposition.

There are nine well known decay channels of the τ lepton. Together they cover the bulk of all τ decays. Of these nine, four are the direct one-prong decays e, μ, π and K plus neutrino(s). The other five final state decay channels involve resonances. They yield a whole spectrum of multi-particle decays, both one- and multi prongs. They are :

Resonance	I	I_3	S	Dominant decay channel
ρ^-	1	-1	0	$\pi\pi$
K^{*-}	$\frac{1}{2}$	$-\frac{1}{2}$	-1	$K\pi$
a_1^-	1	-1	0	$\rho\pi$
K_1^-	$\frac{1}{2}$	$-\frac{1}{2}$	-1	$K^*\pi$
$\rho^-(1700)$	1	-1	0	$\rho\pi\pi$
				$K\bar{K}^*$

Table A.1: Quantum numbers of resonances and their dominant decay modes. Only decay products of τ^- are given. The τ^+ modes are obtained by taking the charge conjugates. S denotes strangeness in this table.

The first channel is the simplest, the ρ meson almost exclusively decays into two pions, i.e. $\rho^\pm \rightarrow \pi^0\pi^\pm$. The decay channels of the other resonances are found by isospin decomposition. Since the K doublets will come in frequently, the relevant quantum numbers are given in table A.2.

$S \setminus I_3$		$I_3 = \frac{1}{2}$	$I_3 = -\frac{1}{2}$		$I_3 = \frac{1}{2}$	$I_3 = -\frac{1}{2}$
$S = 1$	K	K^+	K^0	K^*	K^{*+}	K^{*0}
$S = -1$	$\bar{K}$	$\bar{K}^0$	K^-	$\bar{K}^*$	$\bar{K}^{*0}$	K^{*-}

Table A.2: Relevant quantum numbers for the kaon system.

The decomposition of K^* yields the following channels and their fraction.

$$
\begin{array}{llllll}
K^{*-} & \xrightarrow{\frac{2}{3}} \bar{K}^0\pi^- & \xrightarrow{\frac{1}{2}} K_s^0\pi^- & \xrightarrow{\frac{2}{3}} \pi^\pm\pi^\mp\pi^- & \frac{2}{3}\cdot\frac{1}{2}\cdot\frac{2}{3} = \frac{2}{9} \\
 & & & \xrightarrow{\frac{1}{3}} 2\pi^0\pi^- & \frac{2}{3}\cdot\frac{1}{2}\cdot\frac{1}{3} = \frac{1}{9} \\
 & & \xrightarrow{\frac{1}{2}} K_l^0\pi^- & \longrightarrow K_l^0\pi^- & \frac{2}{3}\cdot\frac{1}{2} = \frac{3}{9} \\
 & \xrightarrow{\frac{1}{3}} \pi^0K^- & & \longrightarrow \pi^0K^- & \frac{1}{3} = \frac{3}{9}
\end{array}
$$

In obtaining the relative contributions, the step $K_s^0 \to \pi\pi$ is approximated by :

$$\pi^\pm\pi^\mp : 2\pi^0 = 2 : 1,$$

whereas the particle data group gives 68.6 : 31.4. The other numbers come from Clebsch Gordan coefficient tables.

The a_1 decays into $\rho\pi$. Therefore, the possible modes are easily obtained.

$$
\begin{array}{llll}
a_1^- & \xrightarrow{\frac{1}{2}} \rho^0\pi^- & \longrightarrow \pi^\pm\pi^\mp\pi^- & \frac{1}{2} \\
a_1^- & \xrightarrow{\frac{1}{2}} \pi^0\rho^- & \longrightarrow 2\pi^0\pi^- & \frac{1}{2}
\end{array}
$$

The allowed isospin decomposition of K_1 is as follows:

$$
\begin{array}{llllllll}
K_1^- & \xrightarrow{\frac{1}{3}} & \pi^0 K^{*-} & \xrightarrow{\frac{2}{3}} & \pi^0 \bar{K}^0 \pi^- & \xrightarrow{\frac{1}{2}} & \pi^0 K_s^0 \pi^- & \xrightarrow{\frac{2}{3}} \pi^0 \pi^{\pm} \pi^{\mp} \pi^- \quad \frac{1}{3}\cdot\frac{2}{3}\cdot\frac{1}{2}\cdot\frac{2}{3} = \frac{2}{27} \\
 & & & & & & & \xrightarrow{\frac{1}{3}} 3\pi^0 \pi^- \quad \frac{1}{3}\cdot\frac{2}{3}\cdot\frac{1}{2}\cdot\frac{1}{3} = \frac{1}{27} \\
 & & & & & \xrightarrow{\frac{1}{2}} & \pi^0 K_l^0 \pi^- & \longrightarrow \pi^0 K_l^0 \pi^- \quad \frac{1}{3}\cdot\frac{2}{3}\cdot\frac{1}{2} = \frac{3}{27} \\
 & & & \xrightarrow{\frac{1}{3}} & 2\pi^0 K^- & & & \longrightarrow 2\pi^0 K^- \quad \frac{1}{3}\cdot\frac{1}{3} = \frac{3}{27} \\
 & \xrightarrow{\frac{2}{3}} & K^{*0} \pi^- & \xrightarrow{\frac{1}{3}} & \pi^0 \bar{K}^0 \pi^- & \xrightarrow{\frac{1}{2}} & \pi^0 K_s^0 \pi^- & \xrightarrow{\frac{2}{3}} \pi^0 \pi^{\pm} \pi^{\mp} \pi^- \quad \frac{2}{3}\cdot\frac{1}{3}\cdot\frac{1}{2}\cdot\frac{2}{3} = \frac{2}{27} \\
 & & & & & & & \xrightarrow{\frac{1}{3}} 3\pi^0 \pi^- \quad \frac{2}{3}\cdot\frac{1}{3}\cdot\frac{1}{2}\cdot\frac{1}{3} = \frac{1}{27} \\
 & & & & & \xrightarrow{\frac{1}{2}} & \pi^0 K_l^0 \pi^- & \longrightarrow \pi^0 K_l^0 \pi^- \quad \frac{2}{3}\cdot\frac{1}{3}\cdot\frac{1}{2} = \frac{3}{27} \\
 & & & \xrightarrow{\frac{2}{3}} & \pi^+ K^- \pi^- & & & \longrightarrow \pi^+ K^- \pi^- \quad \frac{2}{3}\cdot\frac{2}{3} = \frac{12}{27}
\end{array}
$$

Note that modes 1-3 and 5-7 are completely identical in their final states and decay fractions.

The last channel is the $\rho(1700)$. We start with the non-strange channel:

$$
\begin{array}{llllll}
\rho(1700) & \xrightarrow{\frac{1}{2}} & \pi^0 a_1^- & \xrightarrow{\frac{1}{2}} & 2\pi^0 \rho^- & \longrightarrow 3\pi^0 \pi^- \quad \frac{1}{2}\cdot\frac{1}{2} = \frac{1}{4} \\
 & & & \xrightarrow{\frac{1}{2}} & \pi^0 \rho^0 \pi^- & \longrightarrow \pi^0 \pi^{\pm} \pi^{\mp} \pi^- \quad \frac{1}{2}\cdot\frac{1}{2} = \frac{1}{4} \\
 & \xrightarrow{\frac{1}{2}} & a_1^0 \pi^- & \xrightarrow{\frac{1}{2}} & \pi^+ \rho^- \pi^- & \longrightarrow \pi^0 \pi^+ \pi^- \pi^- \quad \frac{1}{2}\cdot\frac{1}{2} = \frac{1}{4} \\
 & & & \xrightarrow{\frac{1}{2}} & \pi^- \rho^+ \pi^- & \longrightarrow \pi^0 \pi^+ \pi^- \pi^- \quad \frac{1}{2}\cdot\frac{1}{2} = \frac{1}{4}
\end{array}
$$

The other mode, $K\bar{K}^*$ yields more final states:

$\rho(1700)$	$\xrightarrow{\frac{1}{2}}$	K^0K^{*-}	$\xrightarrow{\frac{1}{3}}$	$\pi^0K^0K^-$	$\xrightarrow{\frac{1}{2}}$	$\pi^0K_s^0K^-$	$\xrightarrow{\frac{2}{3}}$	$\pi^0\pi^\pm\pi^\mp K^-$	$\frac{1}{2}\cdot\frac{1}{3}\cdot\frac{1}{2}\cdot\frac{2}{3}=\frac{6}{108}$
							$\xrightarrow{\frac{1}{3}}$	$3\pi^0K^-$	$\frac{1}{2}\cdot\frac{1}{3}\cdot\frac{1}{2}\cdot\frac{1}{3}=\frac{3}{108}$
					$\xrightarrow{\frac{1}{2}}$	$\pi^0K_l^0K^-$	$\rightarrow$	$\pi^0K_l^0K^-$	$\frac{1}{2}\cdot\frac{1}{3}\cdot\frac{1}{2}=\frac{9}{108}$
			$\xrightarrow{\frac{2}{3}}$	$2K^0\pi^-$	$\xrightarrow{\frac{1}{2}\cdot\frac{1}{2}}$	$K_s^0K_s^0\pi^-$	$\xrightarrow{\frac{2}{3}\cdot\frac{2}{3}}$	$\pi^\pm\pi^\mp\pi^\pm\pi^\mp\pi^-$	$\frac{1}{2}\cdot\frac{2}{3}\cdot\frac{1}{2}\cdot\frac{1}{2}\cdot\frac{2}{3}\cdot\frac{2}{3}=\frac{4}{108}$
							$\xrightarrow{\frac{2}{3}\cdot\frac{1}{3}}$	$2\pi^0\pi^\pm\pi^\mp\pi^-$	$\frac{1}{2}\cdot\frac{2}{3}\cdot\frac{1}{2}\cdot\frac{1}{2}\cdot\frac{2}{3}\cdot\frac{1}{3}=\frac{2}{108}$
							$\xrightarrow{\frac{1}{3}\cdot\frac{2}{3}}$	$\pi^\pm\pi^\mp2\pi^0\pi^-$	$\frac{1}{2}\cdot\frac{2}{3}\cdot\frac{1}{2}\cdot\frac{1}{2}\cdot\frac{1}{3}\cdot\frac{2}{3}=\frac{2}{108}$
							$\xrightarrow{\frac{1}{3}\cdot\frac{1}{3}}$	$4\pi^0\pi^-$	$\frac{1}{2}\cdot\frac{2}{3}\cdot\frac{1}{2}\cdot\frac{1}{2}\cdot\frac{1}{3}\cdot\frac{1}{3}=\frac{1}{108}$
					$\xrightarrow{\frac{1}{2}\cdot\frac{1}{2}}$	$K_l^0K_s^0\pi^-$	$\xrightarrow{\frac{2}{3}}$	$K_l^0\pi^\pm\pi^\mp\pi^-$	$\frac{1}{2}\cdot\frac{2}{3}\cdot\frac{1}{2}\cdot\frac{2}{3}=\frac{6}{108}$
							$\xrightarrow{\frac{1}{3}}$	$K_l^02\pi^0\pi^-$	$\frac{1}{2}\cdot\frac{2}{3}\cdot\frac{1}{2}\cdot\frac{1}{2}\cdot\frac{1}{3}=\frac{3}{108}$
					$\xrightarrow{\frac{1}{2}\cdot\frac{1}{2}}$	$K_s^0K_l^0\pi^-$	$\xrightarrow{\frac{2}{3}}$	$K_l^0\pi^\pm\pi^\mp\pi^-$	$\frac{1}{2}\cdot\frac{2}{3}\cdot\frac{1}{2}\cdot\frac{1}{2}\cdot\frac{2}{3}=\frac{6}{108}$
							$\xrightarrow{\frac{1}{3}}$	$K_l^02\pi^0\pi^-$	$\frac{1}{2}\cdot\frac{2}{3}\cdot\frac{1}{2}\cdot\frac{1}{2}\cdot\frac{1}{3}=\frac{3}{108}$
					$\xrightarrow{\frac{1}{2}\cdot\frac{1}{2}}$	$2K_l^0\pi^-$	$\rightarrow$	$2K_l^0\pi^-$	$\frac{1}{2}\cdot\frac{2}{3}\cdot\frac{1}{2}\cdot\frac{1}{2}=\frac{9}{108}$
	$\xrightarrow{\frac{1}{2}}$	$K^{*0}K^-$	$\xrightarrow{\frac{1}{3}}$	$\pi^0K^0K^-$	$\xrightarrow{\frac{1}{2}}$	$\pi^0K_s^0K^-$	$\xrightarrow{\frac{2}{3}}$	$\pi^0\pi^\pm\pi^\mp K^-$	$\frac{1}{2}\cdot\frac{1}{3}\cdot\frac{1}{2}\cdot\frac{2}{3}=\frac{6}{108}$
							$\xrightarrow{\frac{1}{3}}$	$3\pi^0K^-$	$\frac{1}{2}\cdot\frac{1}{3}\cdot\frac{1}{2}\cdot\frac{1}{3}=\frac{3}{108}$
					$\xrightarrow{\frac{1}{2}}$	$\pi^0K_l^0K^-$	$\rightarrow$	$\pi^0K_l^0K^-$	$\frac{1}{2}\cdot\frac{1}{3}\cdot\frac{1}{2}=\frac{9}{108}$
			$\xrightarrow{\frac{2}{3}}$	$\pi^-K^+K^-$			$\rightarrow$	$\pi^-K^+K^-$	$\frac{1}{2}\cdot\frac{2}{3}=\frac{36}{108}$

We end this appendix by noting that different resonances may lead to identical final states.

Appendix B

The calculation of $\tau \rightarrow K\nu_\tau$ using a general Lorentz structure

In this appendix we will calculate the decay rates for $\tau \rightarrow K\nu_\tau$ and $K \rightarrow \mu\nu_\mu$ where we allow an additional intermediate boson to mediate the decay, see figure B.1(b). We will include a general Lorentz structure in $\mathcal{M}$. We first will consider the decay $\tau \rightarrow K\nu_\tau$. The particle functions involved are the two Dirac spinors $u_\tau(p)$ and $u_\nu(q)$, and the K scalar $\phi(k)$. The variables in parentheses denote the particle momenta.

We will consider two intermediate bosons. The spin 0 boson with the appropriate propagator:

$$\frac{i}{k^2 - m_V^2} \simeq -\frac{i}{m_V^2} \tag{B.1}$$

and the spin 1 boson:

$$\frac{i(-g^{\mu\nu} + k_\mu k_\nu / m_V^2)}{k^2 - m_V^2} \simeq \frac{ig^{\mu\nu}}{m_V^2} \tag{B.2}$$

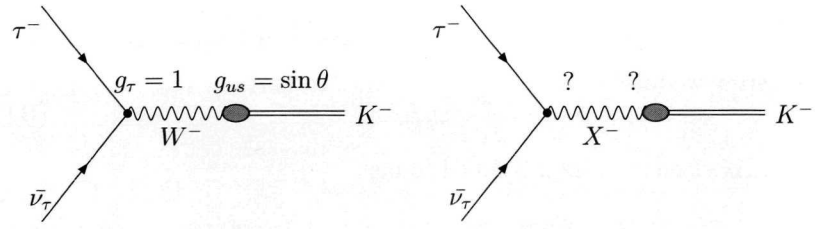

(a) Standard Model interaction

(b) A different scenario

Figure B.1: Standard Model couplings and extensions

where we assumed $m_\tau \ll m_V$. We note here that in our outline the difference between the spin 0 and spin 1 boson is that the latter introduces Lorentz indices and therefore the need for a contraction with Lorentz index carrying objects. Effectively, this leads to the additional factor of m_τ for calculations where the spin 1 boson is involved. The general matrix element reads:

$$\mathcal{M} = G\bar{u}_\tau(p)\,[O]\,u_\nu(q)\psi(k) \tag{B.3}$$

Here, G is a constant.

Before discussing the structure of the vertices, we will make an important observation. For the Lorentz structure O between brackets the five following Lorentz covariant terms can be inserted:

$$1, \gamma^5, \gamma^\mu, \gamma^5\gamma^\mu, \Sigma^{\mu\nu} = \frac{1}{2}\left(\gamma^\mu\gamma^\nu - \gamma^\nu\gamma^\mu\right) \tag{B.4}$$

Where Lorentz indices (i.e. μ) are involved, we have to insert an appropriate quantity to contract with. The only vectors in this problem are p^μ, q^μ and k^μ. It turns out that q^μ always yields 0. p^μ and k^μ give the same result by virtue of $p = q + k$. Whatever combination of the terms in (B.4) we take, we will always end up with unity or γ^5. As an example, consider:

$$\bar{u}_\tau(p)\gamma^\mu u_\nu(q)k_\mu\psi(k) = \bar{u}_\tau(p)\not{k}u_\nu(q)\psi(k) = m_\tau\bar{u}_\tau(p)u_\nu(q)\psi(k) \tag{B.5}$$

where we used:

$$\bar{u}_\tau(p)\not{k}u_\nu(q) = \bar{u}_\tau(p)(\not{p} - \not{q})u_\nu(q) = m_\tau\bar{u}_\tau(p)u_\nu(q) \tag{B.6}$$

Without loss of generality, we can take the following Lorentz structure for the new interaction:

$$\mathcal{M} = G\bar{u}_\tau(p)\left[\alpha + \beta\gamma^5\right]u_\nu(q)\psi(k) \tag{B.7}$$

For the $\tau\nu$-X vertex, we therefore take:

$$-i\frac{g}{2\sqrt{2}}g_\tau\left(\alpha + \beta\gamma^5\right) \tag{B.8}$$

For the X- K vertex we take:

$$-i\frac{g}{2\sqrt{2}}g_{us}f_K \tag{B.9}$$

The squared matrix element in total is found to be:

$$|\mathcal{M}_{tot}|^2 = \frac{1}{16}f_K^2 m_\tau^2\left(2G^2 + 2(\alpha+\beta)FG + (\alpha^2+\beta^2)F^2\right)pq \tag{B.10}$$

The constants F and G are given by:

$$F = \frac{1}{M_X^2}g^2 g_\tau g_{us} \quad G = \frac{1}{M_W^2}g^2\sin\theta_C \tag{B.11}$$

The Standard Model prediction for equation B.10 is found by setting F to zero and substituting equation B.11 for G. A similar expression can be derived for the decay $K \to \mu\nu$:

$$|\mathcal{M}_{tot}|^2 = \frac{1}{16} f_K^2 m_\mu^2 \left(2G^2 + 2(\delta+\varepsilon)GH + (\delta^2+\varepsilon^2)H^2\right) pq \tag{B.12}$$

This time, the Lorentz structure is determined by the parameters δ and ε. The factor G in equation B.12 is given by equation B.11. The factor H is given by:

$$H = \frac{1}{M_X^2} g^2 g_\mu g_{us} \tag{B.13}$$

The total width of both decays can be found through equation 2.4 and we find for the ratio 2.15:

$$R_{\tau/K} = \frac{(2G^2 + 2(\alpha+\beta)FG + (\alpha^2+\beta^2)F^2)}{(2G^2 + 2(\delta+\varepsilon)GH + (\delta^2+\varepsilon^2)H^2)} f(m_\mu, m_K, m_\tau) \tag{B.14}$$

where $f(m_\mu, m_K, m_\tau)$ is defined as:

$$f(m_\mu, m_K, m_\tau) = \frac{m_\tau^3}{2m_\mu^2 m_K} \times \left(\left(\frac{m_K}{m_\tau}\right)^2 \left(\frac{m_\tau^2 - m_K^2}{m_K^2 - m_\mu^2}\right)\right)^2 \tag{B.15}$$

Now, there are a few interesting cases to consider. The first one is an additional interaction of a V-A nature. This we obtain by setting $\alpha = \beta = \delta = \varepsilon = 1$. After substitution B.14 reads:

$$R_{\tau/K} = \frac{\left(\sin\theta_C + g'_\tau g'_{us}\right)^2}{\left(\sin\theta_C + g'_\mu g'_{us}\right)^2} f(m_\mu, m_K, m_\tau) \tag{B.16}$$

The prime indicates a rescaling of the couplings by a factor M_X/M_W. By making the following Taylor expansion:

$$\frac{\left(\sin\theta_C + g'_\tau g'_{us}\right)^2}{\left(\sin\theta_C + g'_\mu g'_{us}\right)^2} \equiv \mathcal{F}(\xi) = \frac{(1+C)^2}{(1+\xi)^2} \tag{B.17}$$

we obtain the following expression for the ratio:

$$R_{\tau/K} = \left(1 + 2\frac{g'_{us}}{\sin\theta_C}(g'_\tau - g'_\mu)\right) f(m_\mu, m_K, m_\tau) \tag{B.18}$$

By inserting the value for f and the measured value for R, we can set a limit on the combination of the new couplings in B.18.

Another possibility is a pure V+A Lorentz structure. The values for the parameters are: $\alpha = \delta = 1 = -\beta = -\varepsilon$. A similar calculation leads to:

$$R_{\tau/K} = \left(1 + \left(\frac{g'_\tau g'_{us}}{\sin\theta_C}\right)^2 - \left(\frac{g'_\mu g'_{us}}{\sin\theta_C}\right)^2\right) f(m_\mu, m_K, m_\tau) \tag{B.19}$$

The last possibility we discuss is a pure V or pure A structure. The relevant parameters are $\alpha = \delta = 1\,, \beta = \varepsilon = 0$ for a pure vector structure, $\alpha = \delta = 0\,, \beta = \varepsilon = 1$ for a pure axial vector structure. In this case, the ratio R becomes:

$$R_{\tau/K} = \left(1 + \frac{g'_{us}}{\sin\theta_C}\left(g'_\tau - g'_\mu\right)\right) f(m_\mu, m_K, m_\tau) \tag{B.20}$$

Bibliography

Bibliography

[1] B.de Wit, J.Smith, *Field theory in particle physics* **Volume I**, North-Holland, Amsterdam 1986

[2] N.Cabibbo, Physical Review Letters **10**, (1963) 531 M.Kobayashi, K.Maskawa, Progress in Theoretical Physics **49**, (1973) 652

[3] Y.S.Tsai, Physical Review **D4**, (1971) 2821

[4] R.Decker, M.Finkemeier, Nuclear Physics **B438**, (1995) 17

[5] P.Abreu et al, Performance of the DELPHI Detector, Nuclear Instruments and Methods, **A378**, (1996) 57

[6] DELPHI-collaboration. DELPHI data analysis package. DELPHI note 89-44, Prog 137 (1989)

[7] S. Jadach et al, The Monte Carlo program KORALZ, for the lepton or quark pair production at LEP/SLC energies: from version 4.0 to version 4.04, CERN-TH/99-119 (and references therein)

[8] M. Feindt, C. Kreuter and O. Podobrin, ELEPHANT Reference Manual, 17 June 1996, DELPHI note 96-82 PROG 217

[9] P.A.Cherenkov, Visible Radiation Produced by Electrons Moving in a Medium with Velocities Exceeding that of Light, Physical Review **52**, (1937) 378

[10] S.Haider, *B_s^0 mixing at the Z^0 resonance determined with the RICH technique*, thesis Rijksuniversiteit of Leiden (1995)

[11] Wei Hao, *Study of Charged Kaon Production in Three-prong Tau Decays*, thesis Rijksuniversiteit of Leiden (1996)

[12] W.Adam et al., Current achievements of the DELPHI Ring Imaging Cherenkov Detector, Nuclear Instruments and Methods, **A371**, (1996) 12

[13] E.G.Anassontzis et al., Nuclear Instruments and Methods, **A323**, (1992) 351

[14] PDG, C. Caso et al., European Physical Journal, C3 (1998) 1

[15] J.M. Lopez et al, A study of charged Kaon production in one-prong Tau decays, DELPHI 99-132 CONF 319, paper nr. 5.563 submitted to the HEP'99 Conference, Tampere, Finland

[16] R. Barate et al, One-prong τ decays with kaons, European Physical Journal, C10 (1999) 1

[17] G. Abbiendi et al, A Study of One-Prong Tau Decays with a Charged Kaon, European Physical Journal, C19 (2001) 653-665

Summary

In this thesis the determination of the branching ratio of single prong kaon production in τ decays is presented. The analysis is based on data taken with the DELPHI detector in the years 1992 through 1995. The DELPHI detector is one of the four experiments of the LEP accelerator at CERN, Geneva.

The theoretical value of the branching ratio of exclusive kaon production in tau decays is calculated using the Standard Model. Since it is not clear how to calculate the coupling of the W boson to the K meson, we used the ratio:

$$R_{\tau/K} = \frac{\Gamma(\tau \rightarrow K\nu_\tau)}{\Gamma(K \rightarrow \mu\nu_\mu)}$$

This way, the contributions of the coupling of the W boson to the K meson cancel. The branching ratio thus calculated yields:

$$BR(\tau \rightarrow K\nu_\tau) = 0.72 \pm 0.01\% \qquad \text{(B.21)}$$

Special attention is paid to possible new interactions which are not present in the Standard Model. Using a general Lorentz structure, branching ratios are calculated for additional interactions. We derive expressions for V-A, V+A, V or A Lorentz structures. Together with the experimental result presented in this thesis, the expressions are used to set limits on possible new interactions.

The main part of this thesis describes the measurement of the branching ratio of single prong kaon production in τ decays. Two subdetectors of the DELPHI detector are highlighted in this thesis. The electromagnetic calorimeter in DELPHI, the HPC, is used for designing a dedicated electron tag in order to free our data set from decays containing electrons. The overall efficiency of this electron tag for identifying electrons is 91.7 %. In 6.5 % of the cases, non-electrons are mistakenly identified as electrons.

The Ring Imaging Cherenkov (RICH) detector plays a paramount role in particle identification, in this thesis in particular to separate kaons from pions and muons on a track-by-track basis. Dictated by the way the RICH is designed to identify particles, and because of the momentum range in which kaons are produced in tau decays, two identification methods are applied; veto identification and ring identification.

The event selection for $e^+e^- \rightarrow \tau^+\tau^-$ is dictated by the kinematical constraints on kaon identification in the RICH. Together with constraints on topology a quite pure

tau sample is obtained. After all selection cuts are applied, the total number of one prong tau decays amounts to 15033 events. The branching ratio is obtained through the ratio:

$$\mathcal{R} = \frac{\text{number of } (\tau \longrightarrow K\nu_\tau)}{\text{number of } (\tau \longrightarrow \mu\nu_\tau\nu_\mu + \tau \longrightarrow \pi\nu_\tau)}$$

Here, the assumption is used that certain systematic uncertainties arising from selection efficiencies, cancel in this ratio. The branching ratio is thus determined to be:

$$BR(\tau \rightarrow K\nu_\tau) = 0.775 \pm 0.074_{stat} \pm 0.055_{sys}$$

The error on the measurement consists of two almost comparable parts arising from statistics and systematics. The errors are dominated by the efficiency to select kaons and by the algorithm to separate veto from positive identification. The result is in agreement with the Standard Model prediction. The errors are larger than the error on the theoretical result, therefore an even more accurate measurement would be meaningful. This however will require a vast increase in statistics to be achieved, for instance in a future 'τ factory'.

Samenvatting

Dit proefschrift beschrijft een meting van de vertakkingsverhouding van het τ lepton dat vervalt in één geladen kaon, en geen andere geladen deeltjes. De vertakkingsverhouding is bepaald aan de hand van data die met de DELPHI detector te Genève in de jaren 1992 tot en met 1995 zijn genomen. De DELPHI detector is één van de vier experimenten opgesteld bij de LEP versneller te Genève.

De theoretische waarde van de vertakkingsverhouding ($\tau \rightarrow K\nu_\tau$) wordt in dit proefschrift berekend aan de hand van het Standaard Model. Omdat de koppeling van het W boson met het K meson niet te berekenen is, is hierbij gebruikt gemaakt van de verhouding:

$$R_{\tau/K} = \frac{\Gamma(\tau \rightarrow K\nu_\tau)}{\Gamma(K \rightarrow \mu\nu_\mu)}$$

De bijdragen van de koppeling van het W boson met het K meson vallen op deze wijze tegen elkaar weg. De vertakkingsverhouding wordt zo bepaald op:

$$BR(\tau \rightarrow K\nu_\tau) = 0.72 \pm 0.01\% \tag{B.22}$$

Additioneel worden mogelijke nieuwe interacties beschouwd die niet in het Standaard Model zijn opgenomen. Hiertoe worden vertakkingsverhoudingen berekend uitgaande van een algemene Lorentz structuur. In het bijzonder wordt gekeken naar nieuwe interacties met de Lorentz structuren V-A, V+A, V of A. De mathematische relaties die hieruit voortkomen, en het meetresultaat van de vervalsbreedte worden gebruikt om een limiet te zetten op mogelijke nieuwe interacties.

Het grootste deel van dit proefschrift gaat over de meting van de vertakkingsverhouding van het τ lepton dat vervalt in één geladen kaon, en geen andere geladen deeltjes. Twee subdetectoren van de voor deze meting gebruikte DELPHI detector worden in het bijzonder toegelicht. De electromagnetische calorimeter van DELPHI, de HPC, wordt gebruikt om specifiek electronen te identificeren met als doel deze vervallen buiten de data selectie te houden. Met de in dit proefschrift beschreven electron identificatie worden 91.7 % van alle electronen geïdentificeerd. In 6.5 % van de gevallen wordt onterecht een ander deeltje als electron geïdentificeerd.

De Ring Imaging Cherenkov (RICH) detector speelt een nog crucialere rol in deeltjes identificatie doordat de detector kaonen kan onderscheiden van pionen en muonen

op individuele basis. Vanwege het karakter van de RICH deeltjes identificatie geeft de impuls waarmee kaonen worden geproduceerd in tau verval, aanleiding tot twee identificatie methoden: de veto identificatie en de positieve identificatie.

Een belangrijk aspect van de analyse die in dit proefschrift wordt gepresenteerd is dat de selectie voor $e^+e^- \rightarrow \tau^+\tau^-$ gebeurtenissen voor een groot deel gebaseerd is op de (kinematische) eis van deeltjes identificatie in de RICH. Samen met de eis dat de gebeurtenis een speciale topologie moet hebben, verkrijgen we al een selectie met een hoog gehalte aan $e^+e^- \rightarrow \tau^+\tau^-$ gebeurtenissen. Na het toepassen van alle selectie eisen beschikken we over 15033 gewenste gebeurtenissen. De vertakkingsverhouding voor de gebeurtenis waarbij een tau vervalt naar één kaon wordt bepaald met behulp van de verhouding:

$$\mathcal{R} = \frac{\text{aantal } (\tau \longrightarrow K\nu_\tau)}{\text{aantal } (\tau \longrightarrow \mu\nu_\tau\nu_\mu + \tau \longrightarrow \pi\nu_\tau)}$$

waarbij we gebruik maken van de aanname dat bepaalde systematische onzekerheden voortkomend uit het rendement van de gebeurtenis selectie, tegen elkaar wegvallen. De zo verkregen vertakkingsverhouding bedraagt:

$$BR(\tau \rightarrow K\nu_\tau) = 0.775 \pm 0.074_{stat} \pm 0.055_{sys}\%$$

De fout op de meting kent een bijna vergelijkbare contributie van het statistische gedeelte en het systematische gedeelte. De totale fout wordt gedomineerd door de efficiency om kaonen te selecteren door de scheiding van veto en positief identificatie gebied. De gemeten waarde voor de vertakkingsverhouding is in overeenstemming met de, met behulp van het Standaard Model berekende waarde. De fout op de meting is echter groter dan de fout op het theoretische resultaat, een nog nauwkeuriger meting is nodig om een verder vergelijk toe te laten. Hiervoor is wel een enorme toename van statistiek benodigd, zoals bijvoorbeeld bij een wellicht toekomstige 'τ factory'.

Acknowledgements

The analysis presented in this thesis could not have been performed without the help and support of many friends and colleagues, and of my family. I thank you for that.

I would like to express my thanks to a few people in particular. First of all I would like to thank Werner Ruckstuhl for introducing me to the subject, and for teaching me the ins and outs of physics analysis. It is sad that you are not here to see the result of it. I thank Jan Timmermans and Peter Kluit for their ever continuing efforts to improve the analysis and this thesis. I thank Jan van Eldik for his friendship, his extensive knowledge of all-time favourite hitsingles, as well for his support in the sometimes unfriendly world of ntuple reading and handling. Jos Engelen does not want te be thanked for reading manuscripts, but I thank him for his ongoing support throughout all the years. And with these people, I would like to thank the Nikhef Institute.

The work presented in this thesis could not have been done without the support of Berenschot, which enabled me to spend time working on my thesis during office hours on moments when it was needed. Thanks as well to all of my colleagues there who never seemed to stop harassing me to finish the thesis.

During my stay in Geneva I made many new friends. Two of them are truly special to me and I would like to thank Michael and Alex for all the crazy moments we have been through.

I thank my family for all their suppport and patience. And last of all, I would like to thank Rosa. I thank her for the nights sitting beside me puzzling about the details of the analysis, for her neverending support during all these years, and for the absolute love she has given me.

Erratum

Op het voorblad van dit proefschrift staat abusievelijk de tijd van 10:45 uur vermeld. Dit moet 11:00 uur zijn.